Detecting vector charge with extreme mass ratio inspirals onto Kerr black holes

Chao Zhang,^a Hong Guo,^b Yungui Gong,^{c,1} and Bin Wang^{d,e,1}

- ^aSchool of Physics and Astronomy, Shanghai Jiao Tong University, 800 Dongchuan Rd, Shanghai 200240, China
- ^bShanghai Frontier Research Center for Gravitational Wave Detection, Shanghai Jiao Tong University, 800 Dongchuan Rd, Shanghai 200240, China
- $^c{\rm School}$ of Physics, Huazhong University of Science and Technology, 1037 LuoYu Rd, Wuhan, Hubei 430074, China
- ^dCenter for Gravitation and Cosmology, Yangzhou University, 88 South Daxue Rd, Yangzhou, Jiangsu 225009, China.
- ^eSchool of Aeronautics and Astronautics, 800 Dongchuan Rd, Shanghai 200240, China E-mail: zhangchao666@sjtu.edu.cn, gh710105@gmail.com, yggong@hust.edu.cn, wang_b@sjtu.edu.cn

Abstract. Extreme mass ratio inspirals (EMRIs) are excellent sources for space-based observatories to explore the properties of black holes and test no-hair theorems. We consider EMRIs with a charged compact object inspiralling onto a Kerr black hole in quasi-circular orbits. Using the Teukolsky and generalized Sasaki-Nakamura formalisms for the gravitational and vector perturbations about a Kerr black hole, we numerically calculate the energy fluxes for both gravitational and vector perturbations induced by a charged particle moving in equatorial circular orbits. With one-year observations of EMRIs, we apply the Fisher information matrix method to estimate the charge uncertainty detected by space-based gravitational wave detectors such as the Laser Interferometer Space Antenna, TianQin, and Taiji, and we find that it is possible to detect vector charges as small as $q \sim 0.0049$. The results show that EMRIs composed of a Kerr black hole with a higher spin a and lighter mass a0, and a secondary charged object with more vector charge give smaller relative error on the charge, thus constrain the charge better. The positive spin of the Kerr black hole can decrease the charge uncertainty by about one or two orders of magnitude.

Keywords: vector charge, gravitational waves, extreme mass ratio inspirals, Kerr black holes

ArXiv ePrint: 2301.05915

¹Corresponding author.

C	ontents	
1	Introduction	1
2	Einstein-Maxwell field equations	3
3	Numerical calculation for the energy flux	6
4	Results	8
5	Parameter Estimation	10
	5.1 Signals5.2 Fisher information matrix	10 14
6	Conclusions	15
\mathbf{A}	Details for Calculating Energy Flux	
	A.1 Generalized Sasaki-Nakamura equation	19
	A.2 The source term	22

1 Introduction

In 2015 the Laser Interferometer Gravitational-Wave Observatory (LIGO) Scientific Collaboration and the Virgo Collaboration [1, 2] directly observed the first gravitational wave (GW) event GW150914 coming from the coalescence of binary black holes (BHs), and the discovery opened us a new window to understand the property of BHs and gravity in the nonlinear and strong field regimes. Until now tens of GW events in the frequency range of tens to hundreds Hertz have been confirmed [3–9]. However, due to the seismic noise and gravity gradient noise, the ground-based GW observatories can only measure transient GWs in the frequency range $10-10^3$ Hz, radiated by the coalescences of stellar-mass compact binaries. Apart from transient GW sources, the future space-based GW detectors like the Laser Interferometer Space Antenna (LISA) [10, 11], TianQin [12] and Taiji [13] will help us uncover unprecedented information about GW sources and fundamental physics [14–18]. One of the most conspicuous sources for the future space-based GW detectors is the extreme mass-ratio inspirals (EMRIs) [19, 20]. EMRIs, which consist of a stellar-mass compact object (secondary object) with mass $m_p \sim 1-100~M_\odot$ such as BHs, neutron stars, white dwarfs, etc. orbiting around a supermassive black hole (SMBH) (primary object) with mass $M \sim$ $10^5 - 10^7 M_{\odot}$, with the mass ratio m_p/M in the range of $10^{-7} - 10^{-4}$, radiate millihertz GWs expected to be observed by the future space-based GW detectors.

Future detections of EMRIs with space-based detectors can provide highly precise measurements on source parameters such as the BH masses, spins, etc. In [21], the authors introduced a family of approximate waveforms for EMRIs to make parameter estimation with LISA. For a typical source of $m_p = 10~M_{\odot}$ and $M = 10^6~M_{\odot}$ with a signal-to-noise ratio (SNR) of 30, LISA can determine the masses of both primary and secondary objects to within a fractional error of $\sim 10^{-4}$, measure the spin of the primary object to within $\sim 10^{-4}$, and localize the source on the sky within $\sim 10^{-3}$ steradians. The improved augmented analytic kludge model [22] provides more accurate and efficient GW waveforms to improve the errors

of parameters by one order of magnitude. Thus, EMRIs can be used to precisely measure the slope of the black-hole mass function [23] or as standard sirens [24] to constrain cosmological parameters and investigate the expansion history of the Universe [25–27]. The observations of EMRIs can also help us explore gravitational physics. For example, they can be used to figure out the spacetime structure around the central SMBH to high precision, allowing us to test if the spacetime geometry is described by general relativity or an alternative theory and analyze the environments such as dark matter surrounding the central SMBH [19, 20, 28–54]. In [55–57], the authors investigated the eccentricity and orbital evolution of BH binaries under the influence of accretion in addition to the scalar/vector and gravitational radiations, and discussed the competition between radiative mechanisms and accretion effects on eccentricity evolution. However, these discussions were mainly based on the Newtonian orbit and dipole emission. A generic, fully-relativistic formalism to study EMRIs in spherically symmetric and non-vacuum BH spacetime was established in [58]. Considering the secondary object of mass m_p orbiting the galactic BHs (GBHs) immersed in an astrophysical environment, like an accretion disk or a dark matter halo, the authors found that the relative flux difference at $\omega M = 0.02$ between a vacuum and a GBH with the halo mass $M_{\rm halo} = 0.1 M$ and the lengthscale $a_0 = 10^2 M_{\rm halo}$ and $10^3 M_{\rm halo}$ is $\sim 10\%$ and 1%, respectively. The results clearly indicate that EMRIs can constrain smaller-scale matter distributions around GBHs [58].

According to the no-hair theorem, any BH can be described by three parameters: the mass, angular momentum, and electric charge. Current observations have not yet been able to confirm the no-hair theorem or the existence of extra fields besides the gravitational fields in modified gravity theories. The coupling between scalar fields and higher-order curvature invariants can invalidate the no-hair theorem so that BHs can carry scalar charge which depends on the mass of BH [59–62]. The possible detection of scalar fields with EMRIs was discussed in [41–46, 63, 64]. Astrophysical BHs are usually assumed to be neutral because of long-time charge dissipation through the presence of the plasma around them or the spontaneous production of electron-positron pairs [65–69]. However, the existence of stable charged astrophysical stellar-mass compact objects such as BHs, neutron stars, white dwarfs, etc. in nature remains controversial [70–77]. There might exist a maximal huge amount of charge with the charge-to-mass ratio of the order one for highly compact stars, whose radius is on the verge of forming an event horizon [71, 72]. The balance between the attractive gravitational force from the matter part and the repulsive force from the electrostatic part is unstable and charged compact stars will collapse to a charged BH due to a decrease in the electric field [78]. BHs can also be charged through the Wald mechanism by selectively accreting charge in a magnetic field [79], or by accreting minicharged dark matter beyond the standard model [80, 81]. The dark photon with mass $\sim 8 \times 10^{-14} \text{ eVc}^{-2}$ is a minimal and well-motivated extension of the standard model for reconciling hydrodynamical simulations with Lyman- α forest absorption line widths at redshift $z \simeq 0.1$ [81–83].

Due to vector radiations, the orbits of EMRIs will be affected, the merger parameters and the merger rate distribution will be affected too [82–84]. The electromagnetic self-force acting on a charged particle in an equatorial circular orbit of Kerr BH was calculated in [38]. It showed the dissipative self-force balances with the sum of the electromagnetic flux radiated to infinity and down the BH horizon, and prograde orbits can stimulate BH superradiance although the superradiance is not sufficient to support floating orbits even at the innermost stable circular orbit (ISCO) [38]. Furthermore, the U(1) charge that is not electromagnetic carried by BHs may bias the parameter estimation of the chirp mass [85]. It was shown that GW150914 is compatible with having charge-to-mass ratio as high as 0.3 [86].

In [50], the energy fluxes for both gravitational and electromagnetic waves induced by a charged particle orbiting around a Schwarzschild BH were studied. It was demonstrated that the electric charge leaves a significant imprint on the phase of GWs and is observable with space-based GW detectors. The estimation accuracy of the charges may reach 10^{-5} by using the analytic kludge (AK) waveform from the inspiral of a charged stellar-mass compact object into a charged massive black hole in the weak-field regime [87]. In this paper, based on the Teukolsky formalism for BH perturbations [88–90], we numerically calculate the energy fluxes for both tensor and vector perturbations induced by a charged particle moving in an equatorial circular orbit around a Kerr BH, the orbital evolution of EMRIs up to the ISCO, and investigate the capabilities to detect vector charges carried by the secondary compact object with space-based GW detectors such as LISA, TianQin, and Taiji. We apply the methods of faithfulness and Fisher information matrix (FIM) to assess the capability of space-based GW detectors to detect the vector charge carried by the secondary compact object. The paper is organized as follows. In Sec. 2, we introduce the model with vector charge and the Teukolsky perturbation formalism. In Sec. 3, we give the source terms as well as procedures for solving the inhomogeneous Teukolsky equations. Then we numerically calculate the energy fluxes for gravitational and vector fields using the Teukolsky and generalized Sasaki-Nakamura (SN) formalisms in the background of a Kerr BH. In Sec. 4, we give the numerical results of energy fluxes falling onto the horizon and radiated to infinity for gravitational and vector fields, then we use the dephasing of GWs to constrain the charge. In Sec. 5, we calculate the faithfulness between GWs with and without vector charge and perform the FIM to estimate the errors of detecting vector charge with LISA, TianQin, and Taiji. Sec. 6 is devoted to conclusions and discussions. In this paper, we set c = G = M = 1.

2 Einstein-Maxwell field equations

The simplest model including vector charges is Einstein-Maxwell theory, which is modeled via the massless vector field

$$S = \int d^4x \frac{\sqrt{-g}}{16\pi} \left[R - \frac{1}{4} F^{\mu\nu} F_{\mu\nu} - A_{\mu} J^{\mu} \right] - S_{\text{matter}}(g_{\mu\nu}, \Phi), \tag{2.1}$$

where R is the Ricci scalar, A_{μ} is a massless vector field, $F_{\mu\nu} = \nabla_{\mu}A_{\nu} - \nabla_{\nu}A_{\mu}$ is the field strength and Φ is the matter field, J^{μ} is the electric current density. Varying the action with respect to the metric tensor and the vector field yields the Einstein-Maxwell field equations

$$G^{\mu\nu} = 8\pi T_p^{\mu\nu} + 8\pi T_e^{\mu\nu},\tag{2.2}$$

$$\nabla_{\nu}F^{\mu\nu} = 4\pi J^{\mu},\tag{2.3}$$

where $G_{\mu\nu}$ is the Einstein tensor, $T_p^{\mu\nu}$ and $T_e^{\mu\nu}$ are the particle's material stress-energy tensor and vector stress-energy tensor, respectively. Since the amplitude of the vector stress-energy $T_e^{\mu\nu}$ is quadratic in the vector field, the contribution to the background metric from the vector field is second order. For an EMRI system $(m_p \ll M)$ composing of a small compact object with mass m_p and charge-to-mass ratio q orbiting around a Kerr BH with mass M and spin Ma, we can ignore the contribution to the background metric from the vector field. The perturbed Einstein and Maxwell equations for EMRIs are

$$G^{\mu\nu} = 8\pi T_n^{\mu\nu},\tag{2.4}$$

$$\nabla_{\nu}F^{\mu\nu} = 4\pi J^{\mu},\tag{2.5}$$

where

$$T_p^{\mu\nu}(x) = m_p \int d\tau \ u^{\mu} u^{\nu} \frac{\delta^{(4)} \left[x - z(\tau) \right]}{\sqrt{-g}},$$
 (2.6)

$$J^{\mu}(x) = q m_p \int d\tau \ u^{\mu} \frac{\delta^{(4)} \left[x - z(\tau) \right]}{\sqrt{-g}}, \tag{2.7}$$

and u^{μ} is the velocity of the particle. We use the Newman-Penrose formalism [91] to study perturbations around a Kerr BH induced by a charged particle with mass m_p and charge q. In Boyer-Lindquist coordinate, the metric of Kerr BHs is

$$ds^{2} = (1 - 2r/\Sigma)dt^{2} + (4ar\sin(\theta)/\Sigma)dtd\varphi - (\Sigma/\Delta)dr^{2} - \Sigma d\theta^{2} - \sin^{2}\theta(r^{2} + a^{2} + 2a^{2}r\sin^{2}\theta/\Sigma)d\varphi^{2}.$$
(2.8)

where $\Sigma = r^2 + a^2 \cos^2 \theta$, and $\Delta = r^2 - 2r + a^2$. When a = 0, the metric reduces to the Schwarzschild metric. Based on the metric (2.8), we construct the null tetrad,

$$l^{\mu} = [(r^{2} + a^{2})/\Delta, 1, 0, a/\Delta],$$

$$n^{\mu} = [r^{2} + a^{2}, -\Delta, 0, a]/(2\Sigma),$$

$$m^{\mu} = [ia\sin\theta, 0, 1, i/\sin\theta]/(2^{1/2}(r + ia\cos\theta)),$$

$$\bar{m}^{\mu} = [-ia\sin\theta, 0, 1, -i/\sin\theta]/(2^{1/2}(r - ia\cos\theta)).$$
(2.9)

The propagating vector field is described by the two complex quantities,

$$\phi_0 = F_{\mu\nu} l^{\mu} m^{\nu}, \qquad \phi_2 = F_{\mu\nu} \bar{m}^{\mu} n^{\nu}.$$
 (2.10)

The propagating gravitational field is described by the two complex Newman-Penrose variables

$$\psi_0 = -C_{\alpha\beta\gamma\delta}l^{\alpha}m^{\beta}l^{\gamma}m^{\delta},
\psi_4 = -C_{\alpha\beta\gamma\delta}n^{\alpha}\bar{m}^{\beta}n^{\gamma}\bar{m}^{\delta},$$
(2.11)

where $C_{\alpha\beta\gamma\delta}$ is the Weyl tensor. A single master equation for tensor (s = -2) and vector (s = -1) perturbations was derived as [88],

$$\left[\frac{(r^2+a^2)^2}{\Delta} - a^2 \sin^2 \theta\right] \frac{\partial^2 \psi}{\partial t^2} + \frac{4ar}{\Delta} \frac{\partial^2 \psi}{\partial t \partial \varphi} + \left[\frac{a^2}{\Delta} - \frac{1}{\sin^2 \theta}\right] \frac{\partial^2 \psi}{\partial \varphi^2}
- \Delta^{-s} \frac{\partial}{\partial r} \left(\Delta^{s+1} \frac{\partial \psi}{\partial r}\right) - \frac{1}{\sin \theta} \frac{\partial}{\partial \theta} \left(\sin \theta \frac{\partial \psi}{\partial \theta}\right) - 2s \left[\frac{a(r-1)}{\Delta} + \frac{i \cos \theta}{\sin^2 \theta}\right] \frac{\partial \psi}{\partial \varphi}
- 2s \left[\frac{(r^2-a^2)}{\Delta} - r - ia \cos \theta\right] \frac{\partial \psi}{\partial t} + (s^2 \cot^2 \theta - s)\psi = 4\pi \Sigma T,$$
(2.12)

the explicit field ψ and the corresponding source T are given in Table 1 [88]. In terms of the eigenfunctions $_sS_{lm}(\theta)$ [88, 92], the field ψ can be written as

$$\psi = \int d\omega \sum_{l,m} R_{\omega lm}(r) \, {}_{s}S_{lm}(\theta) e^{-i\omega t + im\varphi}, \qquad (2.13)$$

s	ψ	T
-1	$(r - ia\cos\theta)^2\phi_2$	$(r - ia\cos\theta)^2 J_2$
-2	$(r - ia\cos\theta)^4\psi_4$	$2(r - ia\cos\theta)^4 T_4$

Table 1. The explicit expressions for the field ψ and the corresponding source T.

where the radial function $R_{\omega lm}(r)$ satisfies the inhomogeneous Teukolsky equation

$$\Delta^{-s} \frac{d}{dr} \left(\Delta^{s+1} \frac{dR_{\omega lm}}{dr} \right) - V_T(r) R_{\omega lm} = T_{\omega lm}, \tag{2.14}$$

the function

$$V_T = -\frac{K^2 - 2is(r-1)K}{\Delta} - 4is\omega r + \lambda_{lm\omega}, \qquad (2.15)$$

 $K = (r^2 + a^2)\omega - am$, $\lambda_{lm\omega}$ is the corresponding eigenvalue which can be computed by the BH Perturbation Toolkit [93], and the source $T_{\omega lm}(r)$ is

$$T_{\omega lm}(r) = \frac{1}{2\pi} \int dt d\Omega \ 4\pi \Sigma T \ _s S_{lm}(\theta) e^{i\omega t - im\varphi}. \tag{2.16}$$

For the equatorial circular trajectory at r_0 under consideration, the sources are

$$T_p^{\mu\nu}(x) = \frac{m_p}{r_0^2} \frac{u^\mu u^\nu}{u^t} \delta(r - r_0) \delta(\cos \theta) \delta(\varphi - \hat{\omega}t),$$

$$J^\mu(x) = q \frac{m_p}{r_0^2} \frac{u^\mu}{u^t} \delta(r - r_0) \delta(\cos \theta) \delta(\varphi - \hat{\omega}t),$$
(2.17)

where $\hat{\omega}$ is the orbital angular frequency. Geodesic motion in Kerr spacetime admits three constants of motion: the specific energy \hat{E} , the angular momentum \hat{L} , and the Carter constant \hat{Q} , and the geodesic equations are

$$m_p \Sigma \frac{dt}{d\tau} = \hat{E} \frac{\varpi^4}{\Delta} + a\hat{L} \left(1 - \frac{\varpi^2}{\Delta} \right) - a^2 \hat{E} \sin^2 \theta, \qquad (2.18)$$

$$m_p \Sigma \frac{dr}{d\tau} = \pm \sqrt{V_r(r_0)},\tag{2.19}$$

$$m_p \Sigma \frac{d\theta}{d\tau} = \pm \sqrt{V_\theta(\theta)},$$
 (2.20)

$$m_p \Sigma \frac{d\varphi}{d\tau} = a\hat{E}\left(\frac{\varpi^2}{\Delta} - 1\right) - \frac{a^2\hat{L}}{\Delta} + \hat{L}\csc^2\theta,$$
 (2.21)

where $\varpi \equiv \sqrt{r^2 + a^2}$, the radial and polar potentials are

$$V_r(r) = \left(\hat{E}\varpi^2 - a\hat{L}\right)^2 - \Delta\left(r^2 + \left(\hat{L} - a\hat{E}\right)^2 + \hat{Q}\right),\tag{2.22}$$

$$V_{\theta}(\theta) = \hat{Q} - \hat{L}^2 \cot^2 \theta - a^2 \left(1 - \hat{E}^2\right) \cos^2 \theta. \tag{2.23}$$

In the adiabatic approximation, for a quasi-circular orbit on the equatorial plane, the coordinates r and θ are considered as constants, then Eqs. (2.18) and (2.21) are the remaining

equations. The conserved constants are [94]

$$\hat{E} = m_p \frac{r_0^{3/2} - 2r_0^{1/2} \pm a}{r_0^{3/4} \left(r_0^{3/2} - 3r_0^{1/2} \pm 2a\right)^{1/2}},$$
(2.24)

$$\hat{L} = m_p \frac{\pm (r_0^2 \mp 2ar_0^{1/2} + a^2)}{r_0^{3/4} \left(r_0^{3/2} - 3r_0^{1/2} \pm 2a\right)^{1/2}},$$
(2.25)

$$\hat{Q} = 0. (2.26)$$

The orbital angular frequency is

$$\hat{\omega} \equiv \frac{d\varphi}{dt} = \frac{\pm 1}{r_0^{3/2} \pm a},\tag{2.27}$$

where \pm corresponds to co-rotating and counter-rotating, respectively. In the following discussions, we use positive a for co-rotating cases and negative a for counter-rotating cases.

3 Numerical calculation for the energy flux

The homogeneous Teukolsky equation (2.14) admits two linearly independent solutions $R_{\omega lm}^{\rm in}$ and $R_{\omega lm}^{\rm up}$, with the following asymptotic values at the horizon r_+ and at infinity,

$$R_{\omega lm}^{\rm in} = \begin{cases} B^{\rm tran} \Delta^{-s} e^{-i\kappa r^*}, & (r \to r_+) \\ B^{\rm out} \frac{e^{i\omega r^*}}{r^{2s+1}} + B^{\rm in} \frac{e^{-i\omega r^*}}{r}, & (r \to +\infty) \end{cases}$$
(3.1)

$$R_{\omega lm}^{\rm up} = \begin{cases} D^{\rm out} e^{i\kappa r^*} + \frac{D^{\rm in}}{\Delta^s} e^{-i\kappa r^*}, & (r \to r_+) \\ D^{\rm tran} \frac{e^{i\omega r^*}}{r^{2s+1}}, & (r \to +\infty) \end{cases}$$
(3.2)

where $\kappa = \omega - ma/(2r_+)$, $r_{\pm} = 1 \pm \sqrt{1-a^2}$, and the tortoise radius of the Kerr metric

$$r^* = r + \frac{2r_+}{r_+ - r_-} \ln \frac{r - r_+}{2} - \frac{2r_-}{r_+ - r_-} \ln \frac{r - r_-}{2}.$$
 (3.3)

The solutions $R_{\omega lm}^{\rm in}$ and $R_{\omega lm}^{\rm up}$ are purely outgoing at infinity and purely ingoing at the horizon. With the help of these homogeneous solutions, the solution to Eq. (2.14) is

$$R_{\omega lm}(r) = \frac{1}{W} \left(R_{\omega lm}^{\rm in} \int_{r}^{+\infty} \Delta^{s} R_{\omega lm}^{\rm up} T_{\omega lm} dr + R_{\omega lm}^{\rm up} \int_{r_{+}}^{r} \Delta^{s} R_{\omega lm}^{\rm in} T_{\omega lm} dr \right). \tag{3.4}$$

with the constant Wronskian given by

$$W = \Delta^{s+1} \left(R_{\omega lm}^{\text{in}} \frac{dR_{\omega lm}^{\text{up}}}{dr} - R_{\omega lm}^{\text{up}} \frac{dR_{\omega lm}^{\text{in}}}{dr} \right) = 2i\omega B^{\text{in}} D^{\text{tran}}.$$
 (3.5)

The solution is purely outgoing at infinity and purely ingoing at the horizon,

$$R_{\omega lm}(r \to r_{+}) = Z_{\omega lm}^{\infty} \Delta^{-s} e^{-i\kappa r^{*}},$$

$$R_{\omega lm}(r \to \infty) = Z_{\omega lm}^{H} r^{-2s-1} e^{i\omega r^{*}},$$
(3.6)

with

$$Z_{\omega lm}^{\infty} = \frac{B^{\text{tran}}}{W} \int_{r_{+}}^{+\infty} \Delta^{s} R_{\omega lm}^{\text{up}} T_{\omega lm} dr,$$

$$Z_{\omega lm}^{H} = \frac{D^{\text{tran}}}{W} \int_{r_{+}}^{+\infty} \Delta^{s} R_{\omega lm}^{\text{in}} T_{\omega lm} dr.$$
(3.7)

For a circular equatorial orbit with orbital angular frequency $\hat{\omega}$, we get

$$Z_{\omega lm}^{H,\infty} = \delta(\omega - m\hat{\omega}) \mathcal{A}_{\omega lm}^{H,\infty}.$$
 (3.8)

For s = -1, the energy fluxes at infinity and the horizon read

$$\dot{E}_{q}^{\infty} = \left(\frac{dE}{dt}\right)_{EM}^{\infty} = \sum_{l=1}^{\infty} \sum_{m=1}^{l} \frac{|\mathcal{A}_{\omega lm}^{H}|^{2}}{\pi},$$

$$\dot{E}_{q}^{H} = \left(\frac{dE}{dt}\right)_{EM}^{H} = \sum_{l=1}^{\infty} \sum_{m=1}^{l} \alpha_{lm}^{E} \frac{|\mathcal{A}_{\omega lm}^{\infty}|^{2}}{\pi},$$
(3.9)

where the coefficient α_{lm}^{E} is [90]

$$\alpha_{lm}^{E} = \frac{128\omega\kappa r_{+}^{3}(\kappa^{2} + 4\epsilon^{2})}{|B_{E}|^{2}}$$
(3.10)

with $\epsilon = \sqrt{1 - a^2}/(4r_+)$ and

$$|B_E|^2 = \lambda_{lm\omega}^2 + 4ma\omega - 4a^2\omega^2. \tag{3.11}$$

For s = -2, the gravitational energy fluxes at infinity and the horizon are given by

$$\dot{E}_{\text{grav}}^{\infty} = \left(\frac{dE}{dt}\right)_{GW}^{\infty} = \sum_{l=2}^{\infty} \sum_{m=1}^{l} \frac{|\mathcal{A}_{\omega lm}^{H}|^{2}}{2\pi\omega^{2}},$$

$$\dot{E}_{\text{grav}}^{H} = \left(\frac{dE}{dt}\right)_{GW}^{H} = \sum_{l=2}^{\infty} \sum_{m=1}^{l} \alpha_{lm}^{G} \frac{|\mathcal{A}_{\omega lm}^{\infty}|^{2}}{2\pi\omega^{2}},$$
(3.12)

where the coefficient α_{lm}^G is [95]

$$\alpha_{lm}^{G} = \frac{256 (2r_{+})^{5} \kappa (\kappa^{2} + 4\epsilon^{2}) (\kappa^{2} + 16\epsilon^{2}) \omega^{3}}{|B_{G}|^{2}},$$
(3.13)

and

$$|B_G|^2 = \left[(\lambda_{lm\omega} + 2)^2 + 4a\omega - 4a^2\omega^2 \right] \times \left[\lambda_{lm\omega}^2 + 36ma\omega - 36a^2\omega^2 \right] + (2\lambda_{lm\omega} + 3) \left[96a^2\omega^2 - 48ma\omega \right] + 144\omega^2 \left(1 - a^2 \right).$$
(3.14)

Therefore, the total energy fluxes emitted from the EMRIs read

$$\dot{E} = \dot{E}_q + \dot{E}_{\text{grav}},\tag{3.15}$$

where

$$\dot{E}_q = \dot{E}_q^{\infty} + \dot{E}_q^H, \quad \dot{E}_{\text{grav}} = \dot{E}_{\text{grav}}^{\infty} + \dot{E}_{\text{grav}}^H. \tag{3.16}$$

The detailed derivation of the above results is given in Appendix A.1. The energy flux emitted by tensor fields can be computed with the BH Perturbation Toolkit [93].

4 Results

The top panel of Fig. 1 shows the normalized vector energy flux $m_p^{-2}M^2\dot{E}_q$ for a charged particle with different charge values of q on a circular orbit about a Kerr BH with the spin a = 0.9, as a function of orbital radius. The vector energy flux is proportional to the square of the vector charge q^2 . The vector energy flux increases as the charged particle inspirals into the central Kerr BH. The ratio between the vector and gravitational energy flux is shown in the bottom panel of Fig. 1. Both the vector and gravitational fluxes are in the same order of $(m_p/M)^2$, the ratio of fluxes is independent of the mass ratio and increases as the orbital radius because the gravitational contribution falls off faster than the vector energy flux at a large orbital radius. Figure 2 shows the normalized vector energy flux $m_n^{-2}M^2\dot{E}_q$ and the ratio of energy fluxes $\dot{E}_q/\dot{E}_{\rm grav}$ as a function of the orbital radius for different values of a. For larger a, the ISCO is smaller, resulting in higher GW frequency at the coalescence. For the same orbital radius, the vector energy flux is slightly larger for smaller a. However, the total energy flux increases with a for one-year observations before the merger due to the smaller ISCO. Figure 3 shows the ratio of energy flux falling onto the horizon to the energy flux radiated away to infinity, as a function of the orbital radius, for various spin a, and for the vector and gravitational fields. It is interesting to note that the sign of ratio becomes negative for Kerr BH with positive a (co-rotating orbit) at a small orbital radius. In these cases, the vector and gravitational fields generate superradiance, leading to extraction of energy from the horizon. The superradiance only happens when the coefficient κ in Eqs. (3.10) and (3.13) becomes negative, which means that the orbital frequency slows down the rotation of the Kerr BH. Our results are consistent with those found in Ref. [38].

The extra energy leakage due to the vector field accelerates the coalescence of binaries. Therefore, we expect the vector charge to leave a significant imprint on the GW phase over one-year evolution before the merger for EMRIs. To detect the vector charge carried by the small compact object in EMRIs, we study the dephasing of GWs caused by the additional energy loss during inspirals. The observation time is one year before the merger,

$$T_{\text{obs}} = \int_{f_{\text{min}}}^{f_{\text{max}}} \frac{1}{\dot{f}} df = 1 \text{ year}, \tag{4.1}$$

where

$$f_{\text{max}} = \min(f_{\text{ISCO}}, f_{\text{up}}), \qquad f_{\text{min}} = \max(f_{\text{low}}, f_{\text{start}}),$$
 (4.2)

 $f = \hat{\omega}/\pi$ is the GW frequency, $f_{\rm ISCO}$ is the frequency at the ISCO [96], $f_{\rm start}$ is the initial frequency at t = 0, the cutoff frequencies $f_{\rm low} = 10^{-4}$ Hz and $f_{\rm up} = 1$ Hz. The orbit evolution is determined by

$$\frac{dr}{dt} = -\dot{E} \left(\frac{d\hat{E}}{dr} \right)^{-1}, \qquad \frac{d\varphi_{\text{orb}}}{dt} = \pi f, \tag{4.3}$$

where $\dot{E} = \dot{E}_q + \dot{E}_{grav}$. The total number of GW cycles accumulated over one year before the merger is [97]

$$\mathcal{N} = \int_{f_{\min}}^{f_{\max}} \frac{f}{\dot{f}} df. \tag{4.4}$$

Considering EMRIs with the mass of the second compact object being fixed to be $m_p = 10 \ M_{\odot}$, we calculate the dephasing $\Delta \mathcal{N} = \mathcal{N}(q=0) - \mathcal{N}(q)$ for different vector charge q, spin a and mass M, and the results are shown in Fig. 4. For one-year observations before

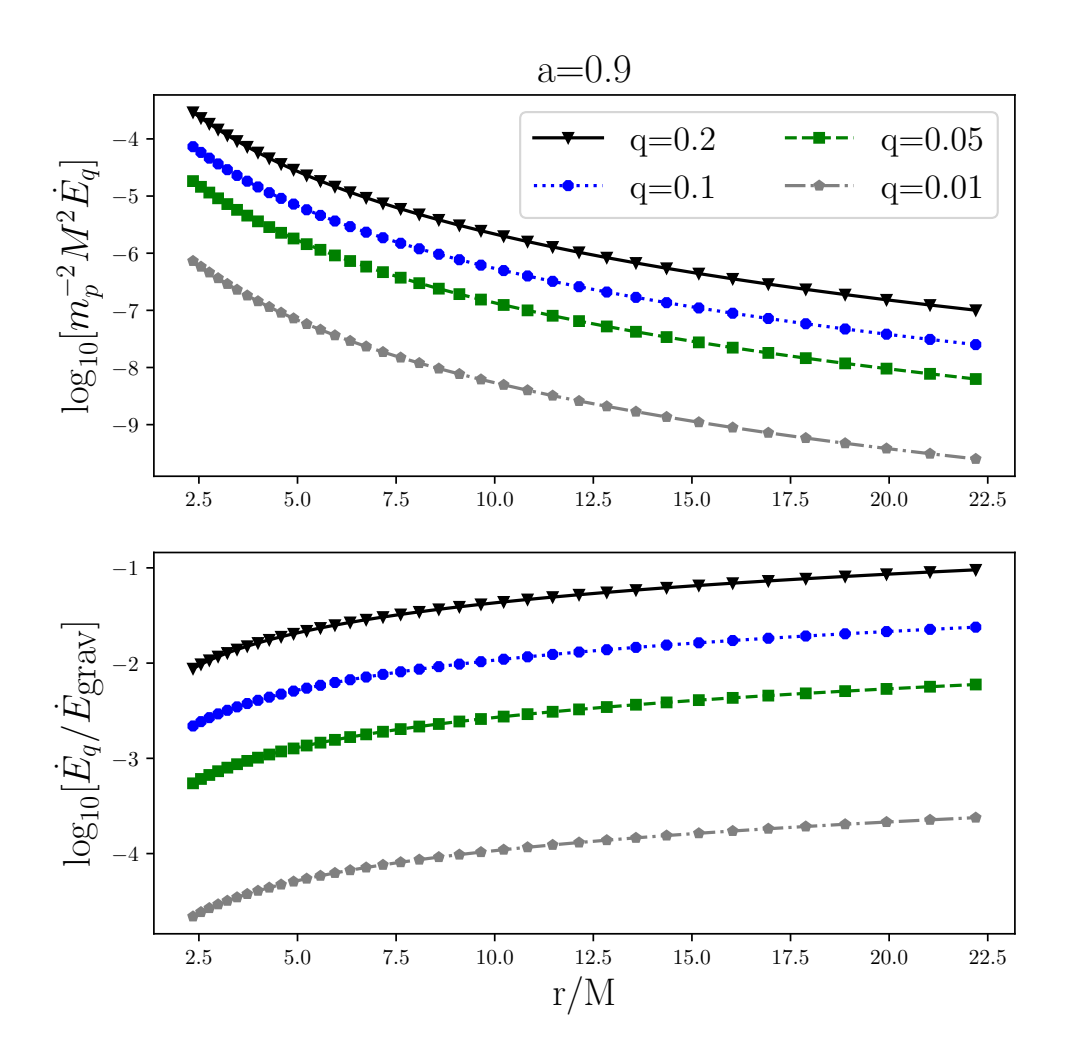


Figure 1. The energy fluxes versus the orbital distance. The top panel shows the vector flux normalized with the mass ratio from a charged particle orbiting around a Kerr BH with the spin of a/M=0.9 for different values of the vector charge q. The bottom panel shows the ratio between vector and gravitational energy fluxes for different values of the vector charge q.

the merger, the charged particle starts further away from ISCO due to extra radiation of the vector field and the difference $\Delta \mathcal{N}$ is always positive. As shown in Fig. 4, $\Delta \mathcal{N}$ increases monotonically with the spin a and the charge-to-mass ratio q, and it strongly depends on the mass of the central BH such that lighter BHs have larger $\Delta \mathcal{N}$. This means that the observations of EMRIs with a lighter and larger-spin Kerr BH can detect the vector charge easier. For the same EMRI configuration in the Kerr background, the co-rotating orbit can detect the vector charge easier than the counter-rotating orbit. Following Refs. [41, 97], we take the threshold for a detectable dephasing that two signals are distinguishable by space-based GW detectors as $\Delta \mathcal{N} = 1$. Observations of EMRIs over one year before the merger may be able to reveal the presence of a vector charge as small as $q \sim 0.007$ for Kerr BHs

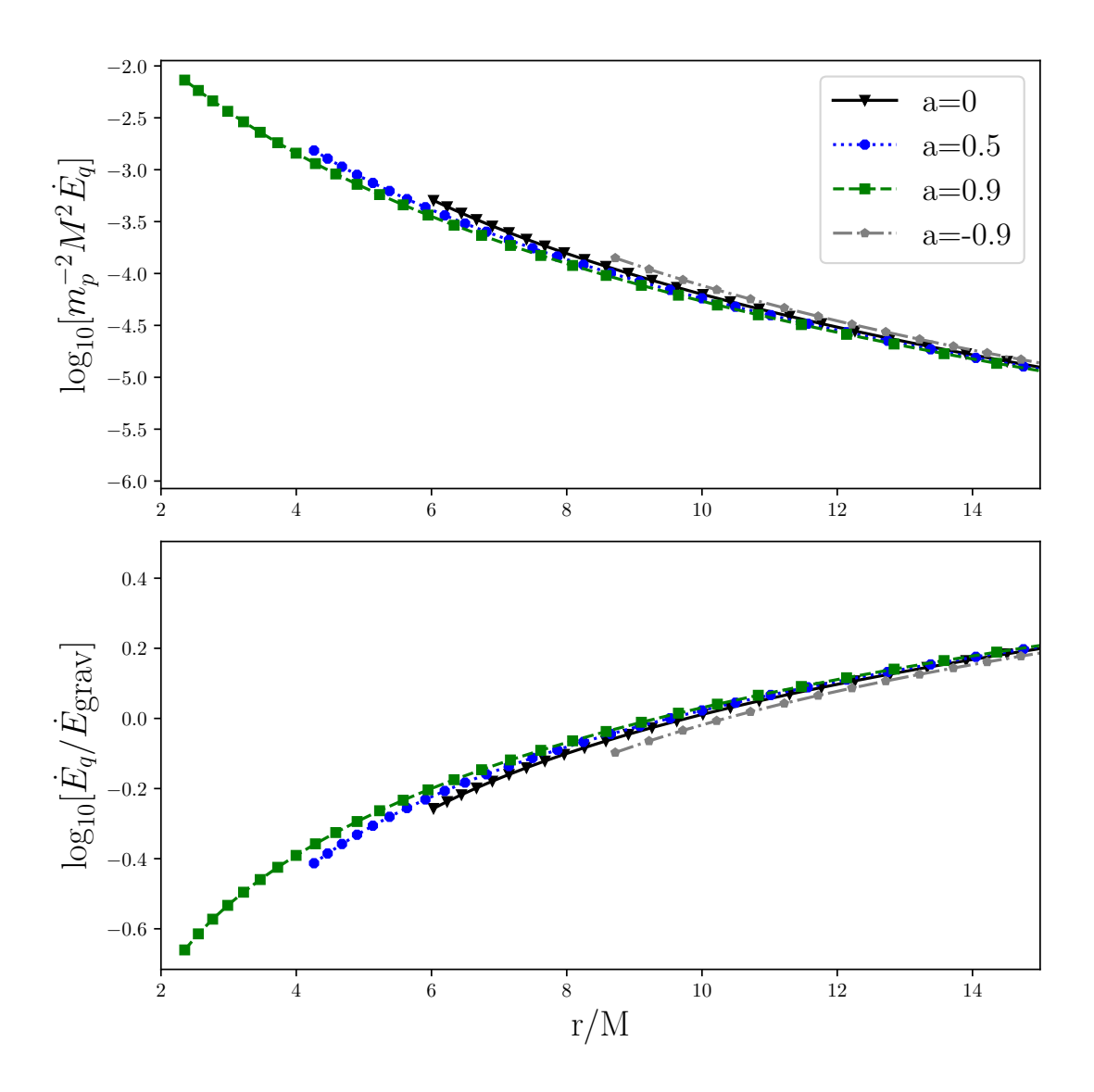


Figure 2. Same as Fig. 1, but for different values of the primary spin a. The vector charge q is set to 1.

with a=0.9 and $M=10^6~M_{\odot}$, and $q\sim0.01$ for Schwarzschild BHs with $M=10^6~M_{\odot}$.

5 Parameter Estimation

To make the analysis more accurate and account for the degeneracy among parameters, we calculate the faithfulness between two GW waveforms and carry out parameter estimation with the FIM method.

5.1 Signals

We can obtain the inspiral trajectory from adiabatic evolution in Eq. (4.3), then compute GWs in the quadrupole approximation. The metric perturbation in the transverse-

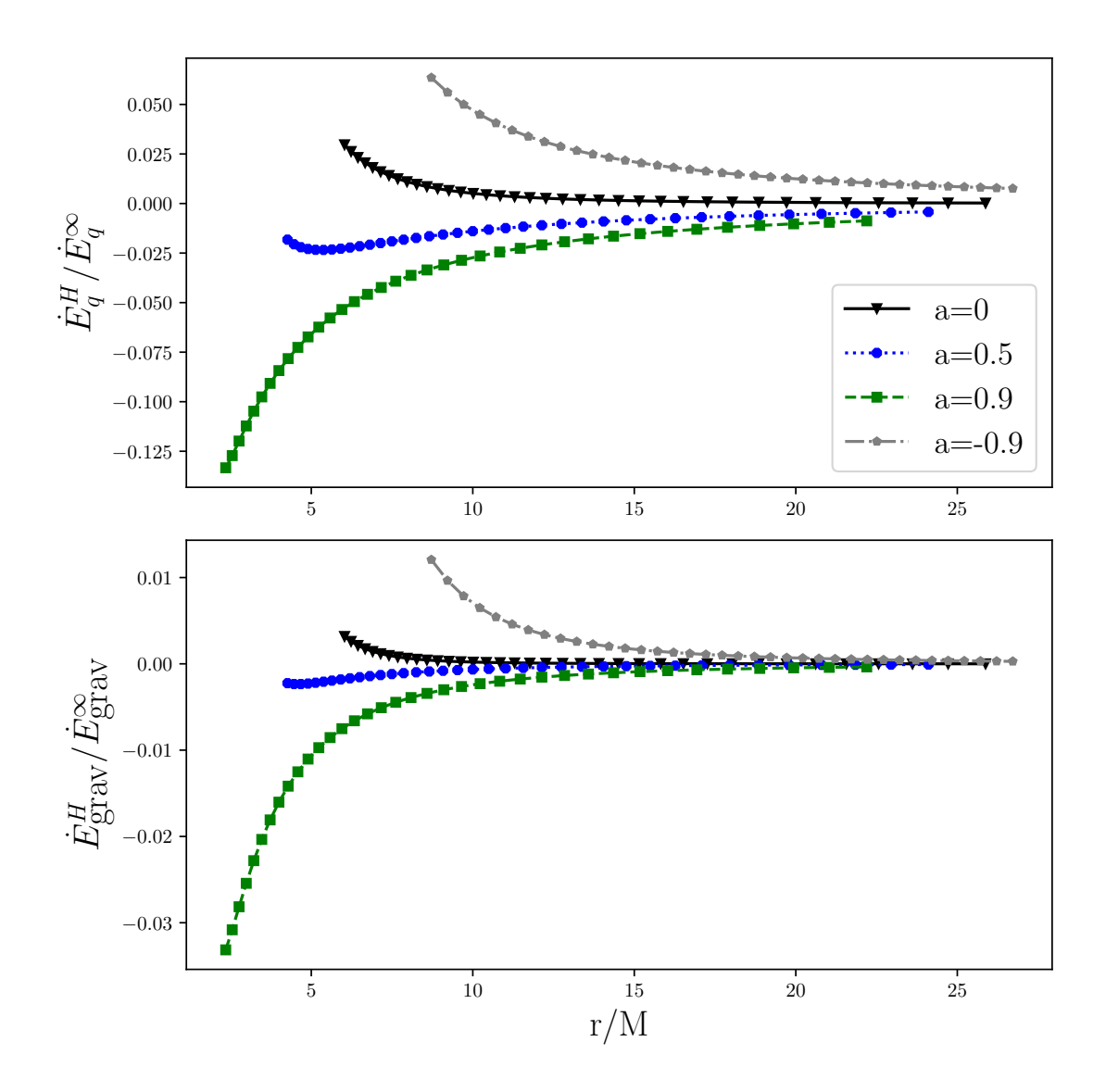


Figure 3. The ratio of the energy flux falling onto the horizon to the energy flux radiated to infinity, as a function of the orbital radius, for various spin a, and for the vector (the top panel) and gravitational cases (the bottom panel).

traceless (TT) gauge is

$$h_{ij}^{\rm TT} = \frac{2}{d_L} \left(P_{il} P_{jm} - \frac{1}{2} P_{ij} P_{lm} \right) \ddot{I}_{lm},$$
 (5.1)

where d_L is the luminosity distance of the source, $P_{ij} = \delta_{ij} - n_i n_j$ is the projection operator acting onto GWs with the unit propagating direction n_j , δ_{ij} is the Kronecker delta function, and \ddot{I}_{ij} is the second time derivative of the mass quadrupole moment. The GW strain measured by the detector is

$$h(t) = h_{+}(t)F^{+}(t) + h_{\times}(t)F^{\times}(t), \tag{5.2}$$

where $h_{+}(t) = A \cos \left[2\varphi_{\rm orb} + 2\varphi_{0}\right] \left(1 + \cos^{2}\iota\right)$, $h_{\times}(t) = -2A \sin \left[2\varphi_{\rm orb} + 2\varphi_{0}\right] \cos \iota$, ι is the inclination angle between the binary orbital angular momentum and the line of sight, the GW

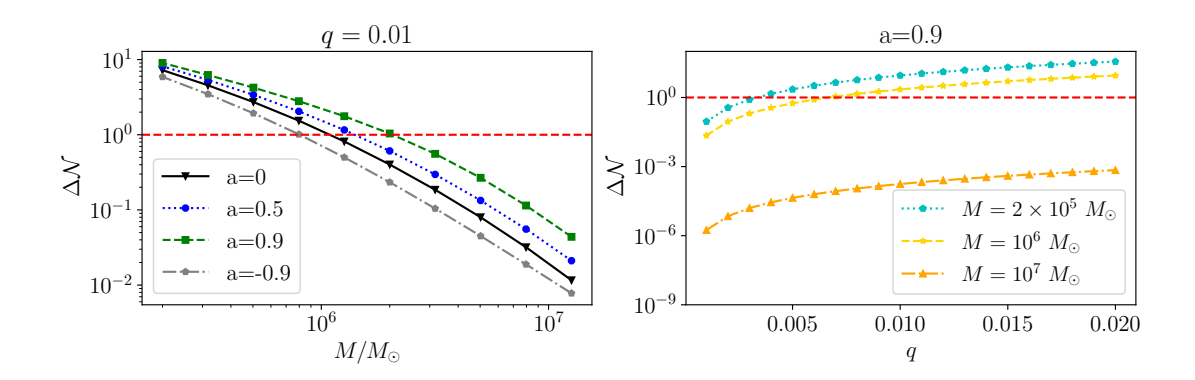


Figure 4. The difference between the number of GW cycles accumulated by EMRIs with and without the vector charge in circular orbits. The left panel shows the dephasing as a function of the mass of the Kerr BH in the range $M \in \left[2 \times 10^5, 2 \times 10^7\right] M_{\odot}$ for different spin values, the charge q = 0.01. The right panel shows the dephasing as a function of the charge-to-mass ratio q for different M, the spin a = 0.9. The red dashed line corresponds to the threshold above which two signals are distinguishable with space-based GW detectors. All observational time is one year before the merger.

amplitude $\mathcal{A} = 2m_{\rm p} \left[M\hat{\omega}(t)\right]^{2/3}/d_L$ and φ_0 is the initial phase. The interferometer pattern functions $F^{+,\times}(t)$ and ι can be expressed in terms of four angles which specify the source orientation, (θ_s, ϕ_s) , and the orbital angular direction (θ_1, ϕ_1) . The faithfulness between two signals is defined as

$$\mathcal{F}_n[h_1, h_2] = \max_{\{t_c, \phi_c\}} \frac{\langle h_1 | h_2 \rangle}{\sqrt{\langle h_1 | h_1 \rangle \langle h_2 | h_2 \rangle}} , \qquad (5.3)$$

where (t_c, ϕ_c) are time and phase offsets [98], the noise-weighted inner product between two templates h_1 and h_2 is

$$\langle h_1 | h_2 \rangle = 4\Re \int_{f_{\min}}^{f_{\max}} \frac{\tilde{h}_1(f)\tilde{h}_2^*(f)}{S_n(f)} df,$$
 (5.4)

 $h_1(f)$ is the Fourier transform of the time-domain signal h(t), its complex conjugate is $h_1^*(f)$, and $S_n(f)$ is the noise spectral density for space-based GW detectors. The signal-to-noise ratio (SNR) can be obtained by calculating $\rho = \langle h|h\rangle^{1/2}$. The sensitivity curves of LISA, TianQin, and Taiji are shown in Fig. 5. As pointed out in [99], two signals can be distinguished by LISA if $\mathcal{F}_n \leq 0.988$. Here we choose the source masses $m_p = 10 \ M_{\odot}$, $M = 10^6 \ M_{\odot}$, the source angles $\theta_s = \pi/3$, $\phi_s = \pi/2$ and $\theta_1 = \phi_1 = \pi/4$, the luminosity distance is scaled to ensure SNR $\rho = 30$, the initial phase is set as $\varphi_0 = 0$ and the initial orbital separation is adjusted to experience one-year adiabatic evolution before the plunge $r_{\rm end} = r_{\rm ISCO} + 0.1~M$. In Fig. 6, we show the faithfulness between GW signals with and without the vector charge for LISA as a function of the vector charge. The results show that one-year observations of EM-RIs with LISA may be able to reveal the presence of a vector charge as small as $q \sim 0.002$ for Kerr BHs with a = 0.9 and $M = 10^6 M_{\odot}$ (co-rotating orbit), $q \sim 0.003$ for Schwarzschild BHs with a = 0 and $M = 10^6 M_{\odot}$, and $q \sim 0.004$ for Kerr BHs with a = -0.9 and $M = 10^6 M_{\odot}$ (counter-rotating orbit). Larger positive spin of the Kerr BH (co-rotating orbit) can help us detect the vector charge easier, which is consistent with the results obtained from the dephasing in the previous section.

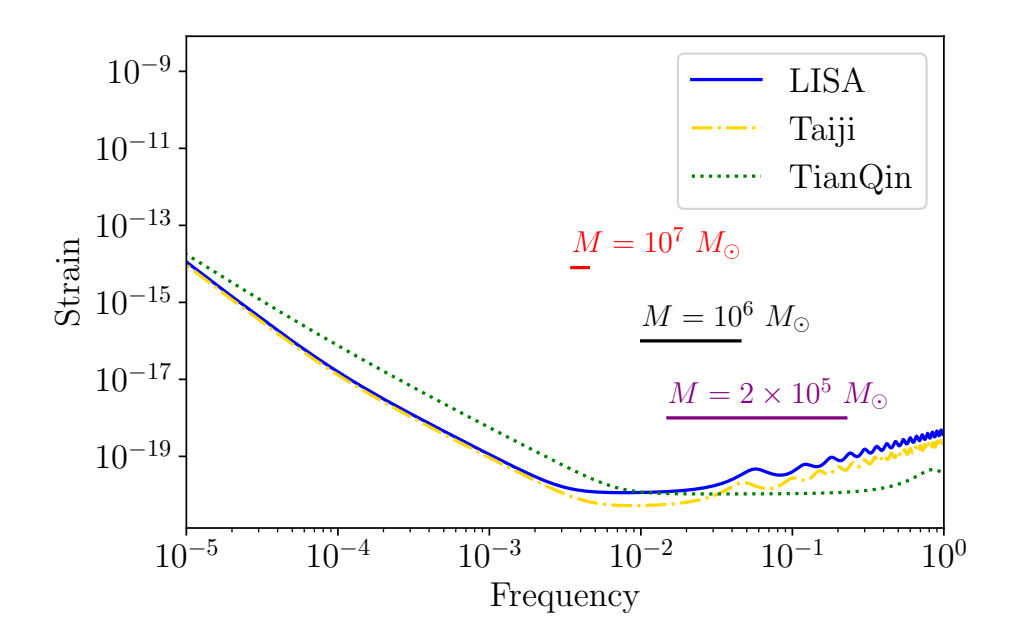


Figure 5. The sensitivity curves for LISA, TianQin, and Taiji. The horizontal solid lines represent the frequency band $f_{\rm start}$ to $f_{\rm ISCO}$ for EMRIs with a=0.9, and $M=2\times 10^5~M_{\odot}$, $M=10^6~M_{\odot}$ and $M=10^7~M_{\odot}$ over one-year evolution before the merger.

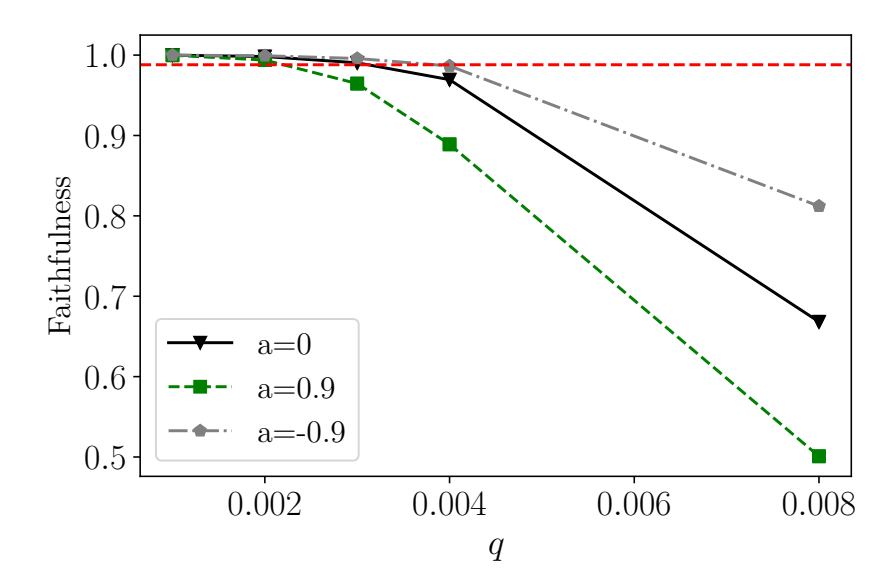


Figure 6. Faithfulness between GW signals with and without the vector charge for LISA as a function of the charge q. The spin of the Kerr BH is a=0, a=0.9, and a=-0.9. The horizontal dashed line represents the detection limit with LISA, $\mathcal{F}_n=0.988$.

5.2 Fisher information matrix

The signals (5.2) measured by the detector are determined by the following eleven parameters

$$\xi = (\ln M, \ln m_p, a, q, r_0, \varphi_0, \theta_s, \phi_s, \theta_1, \phi_1, d_L). \tag{5.5}$$

In the large SNR limit, the posterior probability distribution of the source parameters ξ can be approximated by a multivariate Gaussian distribution centered around the true values $\hat{\xi}$. Assuming flat or Gaussian priors on the source parameters ξ , their covariances are given by the inverse of the FIM

$$\Gamma_{ij} = \left\langle \frac{\partial h}{\partial \xi_i} \middle| \frac{\partial h}{\partial \xi_j} \right\rangle_{\xi = \hat{\xi}}.$$
(5.6)

The statistical error on ξ and the correlation coefficients between the parameters are provided by the diagonal and non-diagonal parts of $\Sigma = \Gamma^{-1}$, i.e.

$$\sigma_i = \Sigma_{ii}^{1/2} \quad , \quad c_{\xi_i \xi_j} = \Sigma_{ij} / \left(\sigma_{\xi_i} \sigma_{\xi_j} \right).$$
 (5.7)

Because of the triangle configuration of the space-based GW detector, the total SNR is defined by $\rho = \sqrt{\rho_1^2 + \rho_2^2}$, so the total covariance matrix of the binary parameters is obtained by inverting the sum of the Fisher matrices $\sigma_{\xi_i}^2 = (\Gamma_1 + \Gamma_2)_{ii}^{-1}$. Here we fix the source angles $\theta_s = \pi/3$, $\phi_s = \pi/2$ and $\theta_1 = \phi_1 = \pi/4$, the initial phase is set as $\varphi_0 = 0$ and the initial orbital separation is adjusted to experience one-year adiabatic evolution before the plunge $r_{\rm end} = r_{\rm ISCO} + 0.1~M$. The luminosity distance d_L is set to be 1 Gpc. We apply the FIM method for LISA, TianQin, and Taiji to estimate the errors of the vector charge.

The relative errors of the vector charge q as a function of the vector charge with LISA, TianQin and Taiji are shown in Fig. 7. For one-year observations before the merger, the charged particle starts further away from ISCO due to extra radiation of the vector field, so the 1σ error for the charge decreases with the charge q. For EMRIs with $M=2\times10^5~M_{\odot}$ and a = 0.9, as shown in the top panel, the relative errors of the charge q with TianQin are better than LISA and Taiji. For $M=10^6~M_{\odot}$ and a=0.9 as shown in the middle panel, the relative errors of the charge q with TianQin and LISA are almost the same. For $M=10^7~M_{\odot}$ and a = 0.9 as shown in the bottom panel, the relative errors of the charge q with TianQin are worse than LISA and Taiji. In all the cases, the relative errors of the charge q with Taiji are better than LISA, for the reason that the sensitivity of Taiji is always better than LISA. For $M = 2 \times 10^5 M_{\odot}$ and a = 0.9, the relative errors with TianQin are better than LISA and Taiji since the sensitivity of TianQin is better than LISA and Taiji in the high-frequency band, but worse than LISA and Taiji in the low-frequency band as shown in Fig. 5. For EMRIs with $m_p = 10 \ M_{\odot}$, $M = 10^6 \ M_{\odot}$ and a = 0.9, the vector charge can be constrained for LISA as small as $q \sim 0.021$, for TianQin as small as $q \sim 0.028$ and for Taiji as small as $q \sim 0.016$. For EMRIs with $m_p = 10~M_{\odot},~M = 2 \times 10^5~M_{\odot}$ and a = 0.9, the vector charge can be constrained for LISA as small as $q \sim 0.0082$, for TianQin as small as $q \sim 0.0049$ and for Taiji as small as $q \sim 0.0057$.

Figure 8 shows the relative errors of the vector charge q versus the spin a with LISA, TianQin, and Taiji. In general, the relative errors of the charge for the co-rotating orbit are better than those for the counter-rotating orbit. We only consider the co-rotating orbit for simplicity. The 1σ error for the charge decreases with the spin a. Comparing the relative errors for Kerr BHs with spin a=0.9 and spin a=0, we find that the spin of Kerr BHs can decrease the charge uncertainty by about one or two orders of magnitude, depending

on the mass of the Kerr BH. For EMRIs with $M=10^6~M_{\odot},~m_p=10~M_{\odot},~q=0.05,$ and different a, the corner plots for source parameters with LISA are shown in Figs. 9, 10 and 11. For comparison, we also show the corner plot for charged EMRIs in the Schwarzschild BH background in Fig. 12. For a=(0.9,0,-0.9), the corresponding errors of charge σ_q are (0.0031,0.086,0.65), respectively. As expected, σ_q is smaller for co-rotating orbits and bigger for counter-rotating orbits. For EMRIs in the Kerr background, the co-rotating orbit can better detect the vector charge. It is interesting to note that the charge q are anticorrelated with the mass M and the spin a of Kerr BHs, and the correlations between q and M, and q and m_p in the Kerr BH background are opposite to those in the Schwarzschild BH background.

6 Conclusions

We study the energy emissions and GWs from EMRIs consisting of a small charged compact object with mass m_p and the charge to mass ratio q inspiraling into a Kerr BH with spin a. We derive the formula for solving the inhomogeneous Teukolsky equation with a vector field and calculate the power emission due to the vector field in the Kerr background. By using the difference between the number of GW cycles $\Delta \mathcal{N}$ accumulated by EMRIs with and without the vector charge in circular orbits over one year before the merger, we may reveal the presence of a vector charge as small as $q \sim 0.007$ for Kerr BHs with a = 0.9 and $M = 10^6 M_{\odot}$, and $q \sim 0.01$ for Schwarzschild BHs with $M = 10^6 M_{\odot}$. The dephasing increases monotonically with the charge-to-mass ratio q, and it strongly depends on the mass of the Kerr BH such that lighter BHs have larger dephasing.

We also apply the faithfulness between GW signals with and without the vector charge to discuss the detection of the vector charge q. We find that positive larger spin of the Kerr BH can help us detect the vector charge easier. We show that one-year observations of EMRIs with LISA may be able to reveal the presence of a vector charge as small as $q \sim 0.002$ for Kerr BHs with a=0.9 and $M=10^6~M_{\odot},~q\sim 0.003$ for Schwarzschild BHs with a=0 and $M=10^6~M_{\odot}$, and $q\sim 0.004$ for Kerr BHs with a=-0.9 and $M=10^6~M_{\odot}$.

To determine vector charge more accurately and account for the degeneracy among parameters, we calculate the FIM to estimate the errors of the vector charge q. For EMRIs with $M=2\times 10^5~M_{\odot}$ and a=0.9, the vector charge q can be constrained as small as $q \sim 0.0049$ with TianQin, $q \sim 0.0057$ with Taiji, and $q \sim 0.0082$ with LISA. For EMRIs with $M=10^6~M_{\odot}$ and a=0.9, the vector charge can be constrained as small as $q\sim0.016$ with Taiji, $q \sim 0.021$ with LISA, and $q \sim 0.028$ with TianQin. Since the sensitivity of TianQin is better than LISA and Taiji in the high-frequency bands, the ability to detect the vector charge for TianQin is better than LISA and Taiji when the mass M of the Kerr BH with a = 0.9 is lighter than $\sim 2 \times 10^5 \ M_{\odot}$. For the mass M of the Kerr BH with a = 0.9 above $10^6 \ M_{\odot}$, LISA and Taiji are more likely to detect smaller vector charges. The relative errors of the charge qwith Taiji are always smaller than LISA because the sensitivity of Taiji is always better than LISA. Due to the extra radiation of the vector field, the charged particle starts further away from ISCO, so the 1σ error for the charge decreases with the charge q. As the spin a of Kerr BHs increases, the ISCO becomes smaller, the positive spin of Kerr BHs (co-rotating) can decrease the charge uncertainty by about one or two orders of magnitude, depending on the mass of the Kerr BH. For EMRIs with $M=10^6~M_\odot,~m_p=10~M_\odot,~q=0.05,$ and different a = (0.9, 0, -0.9), the corresponding errors of charge σ_q with LISA are (0.0031, 0.086, 0.65), respectively, so co-rotating orbits can better detect the vector charge. It is interesting to

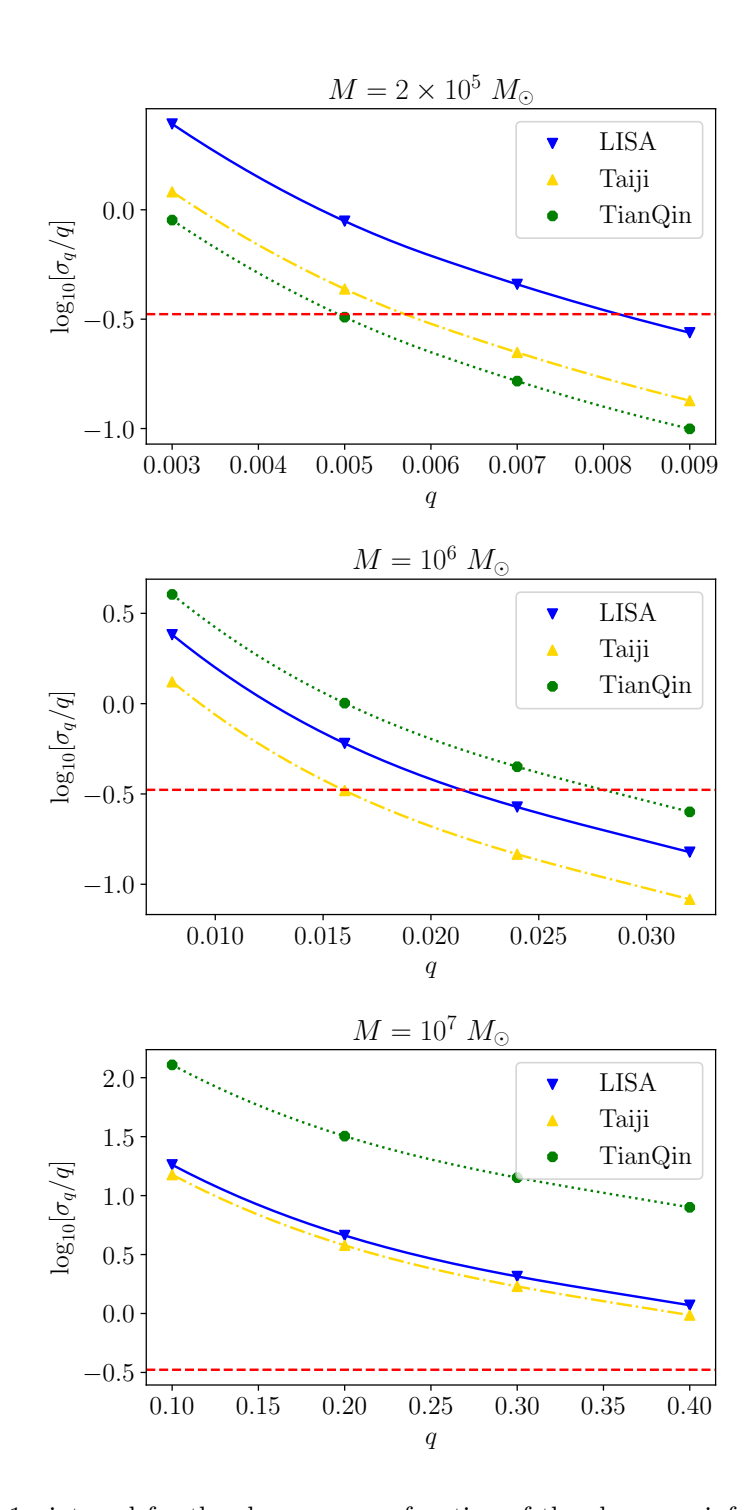


Figure 7. The 1σ interval for the charge q as a function of the charge q, inferred after one-year observations of EMRI with a=0.9 and different M with LISA, Taiji, and TianQin. The horizontal dashed lines represent the 3σ limit 33.3%.

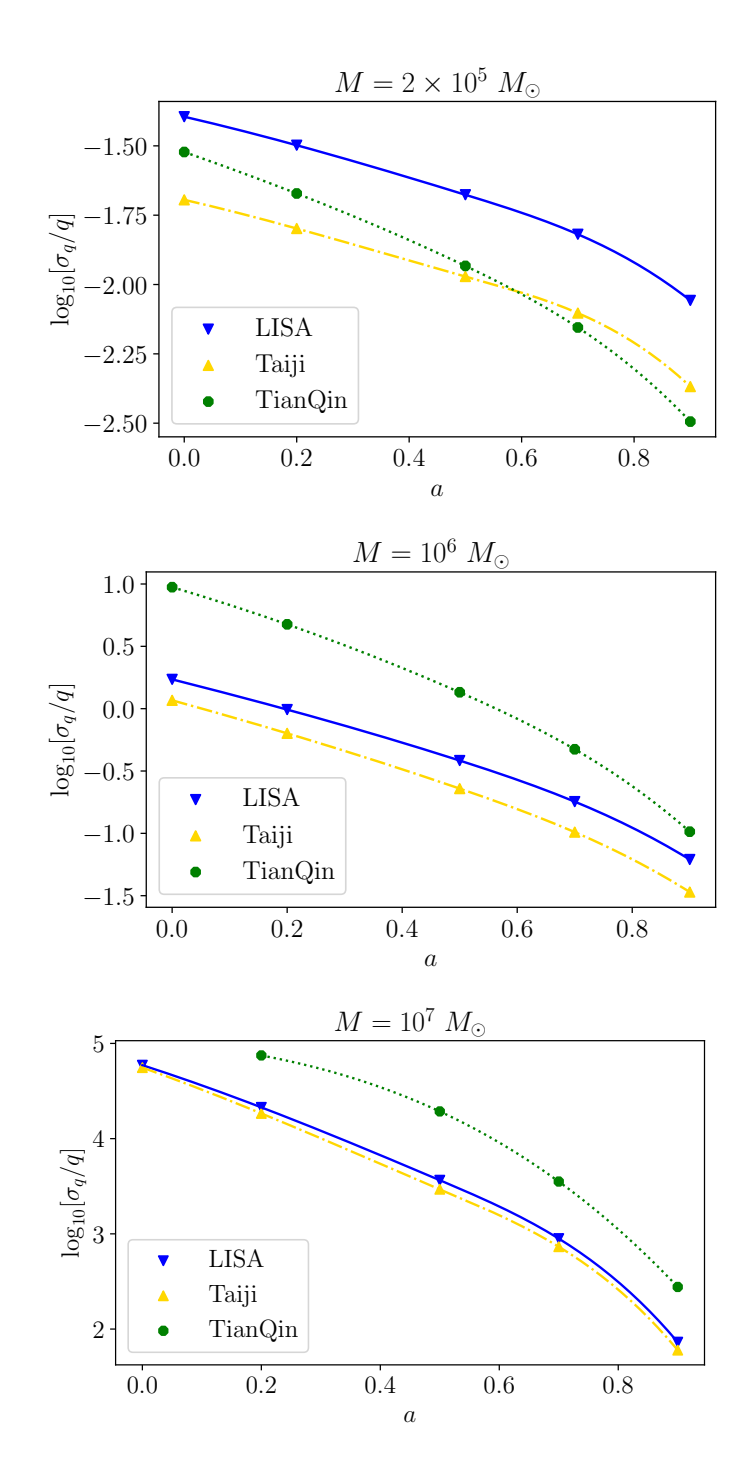


Figure 8. The 1σ interval for the charge q as a function of the spin a, inferred after one-year observations of EMRI with q=0.05 and different M with LISA, Taiji, and TianQin.

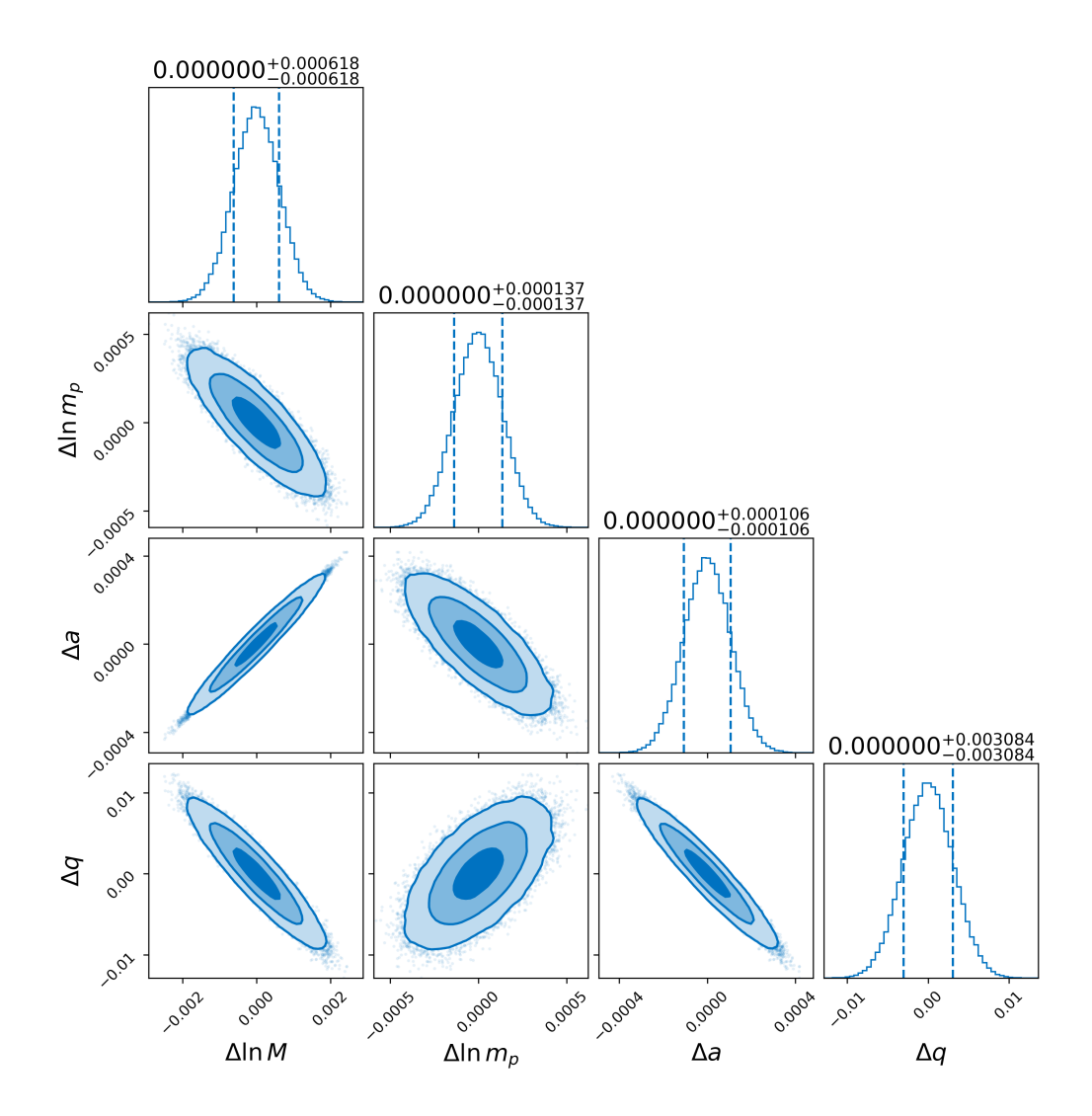


Figure 9. Corner plot for the probability distribution of the source parameters ($\ln M$, $\ln m_p$, a, q) with LISA, inferred after one-year observations of EMRIs with q=0.05 and a=0.9. Vertical lines show the 1σ interval for the source parameter. The contours correspond to the 68%, 95%, and 99% probability confidence intervals.

note that the charge q are anti-correlated with the mass M and the spin a of Kerr BHs, and the correlations between q and M, and q and m_p in the Kerr BH background are opposite to those in the Schwarzschild BH background. In summary, the observations of EMRIs with a lighter and larger-spin Kerr BH can detect the vector charge easier.

Acknowledgments

This work makes use of the Black Hole Perturbation Toolkit package. This research is supported in part by the National Key Research and Development Program of China under Grant No. 2020YFC2201504.

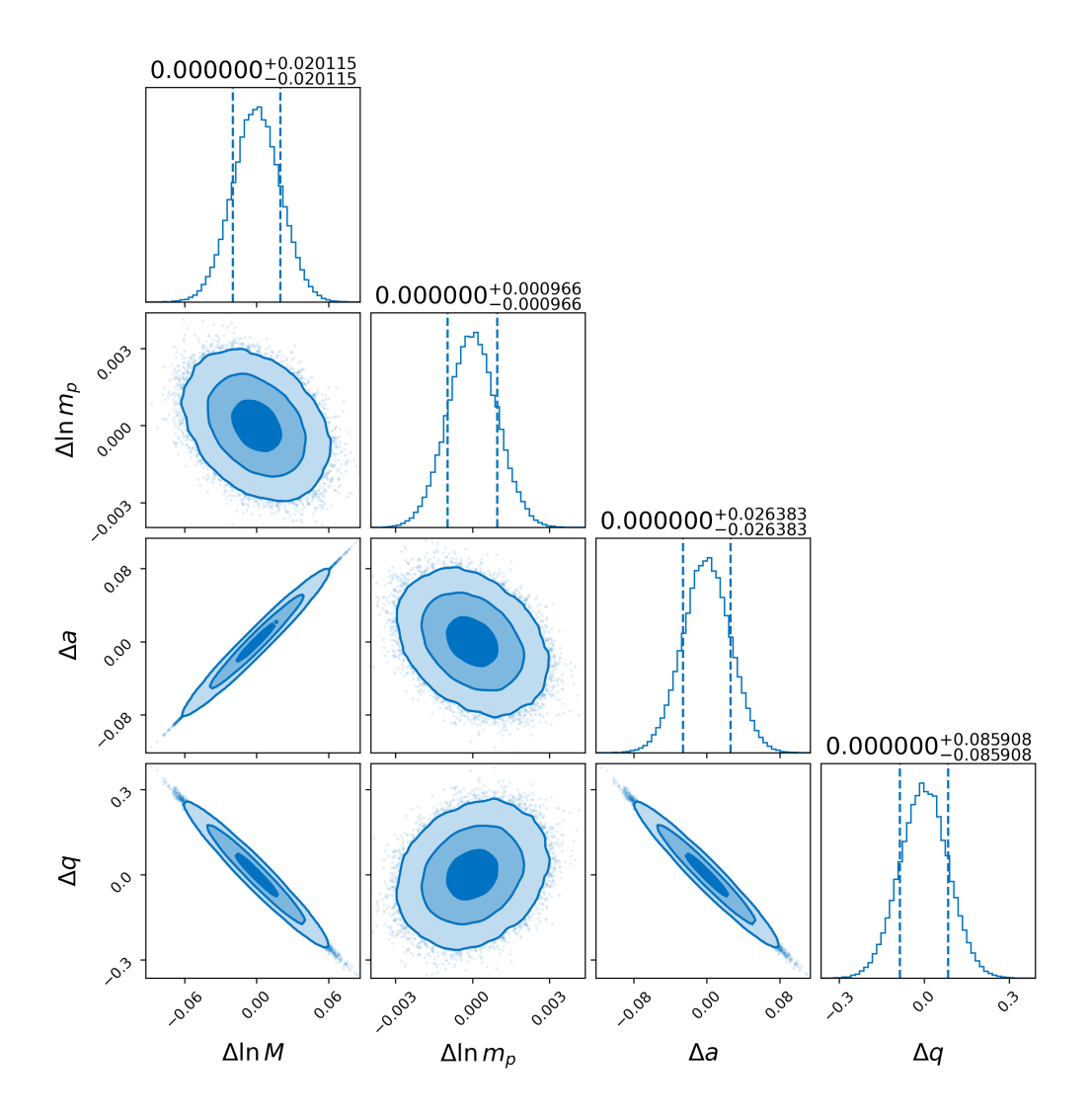


Figure 10. Corner plot for the probability distribution of the source parameters $(\ln M, \ln m_p, a, q)$ with LISA, inferred after one-year observations of EMRIs with q=0.05 and a=0. Vertical lines show the 1σ interval for the source parameter. The contours correspond to the 68%, 95%, and 99% probability confidence intervals.

A Details for Calculating Energy Flux

A.1 Generalized Sasaki-Nakamura equation

In this appendix, we provide further technical details on the formalisms that we compute the vector flux. The generalized Sasaki-Nakamura equation is given by [100]

$$\frac{d^2X}{dr^{*2}} - {}_sF(r)\frac{dX}{dr^*} - {}_sU(r)X = 0, (A.1)$$

where $dr/dr^* = f(r) = \Delta/(r^2 + a^2)$. The coefficient $_sF(r)$ is

$$_{s}F(r) = \frac{\eta(r)_{,r}}{\eta(r)} \frac{\Delta}{r^2 + a^2},$$
 (A.2)

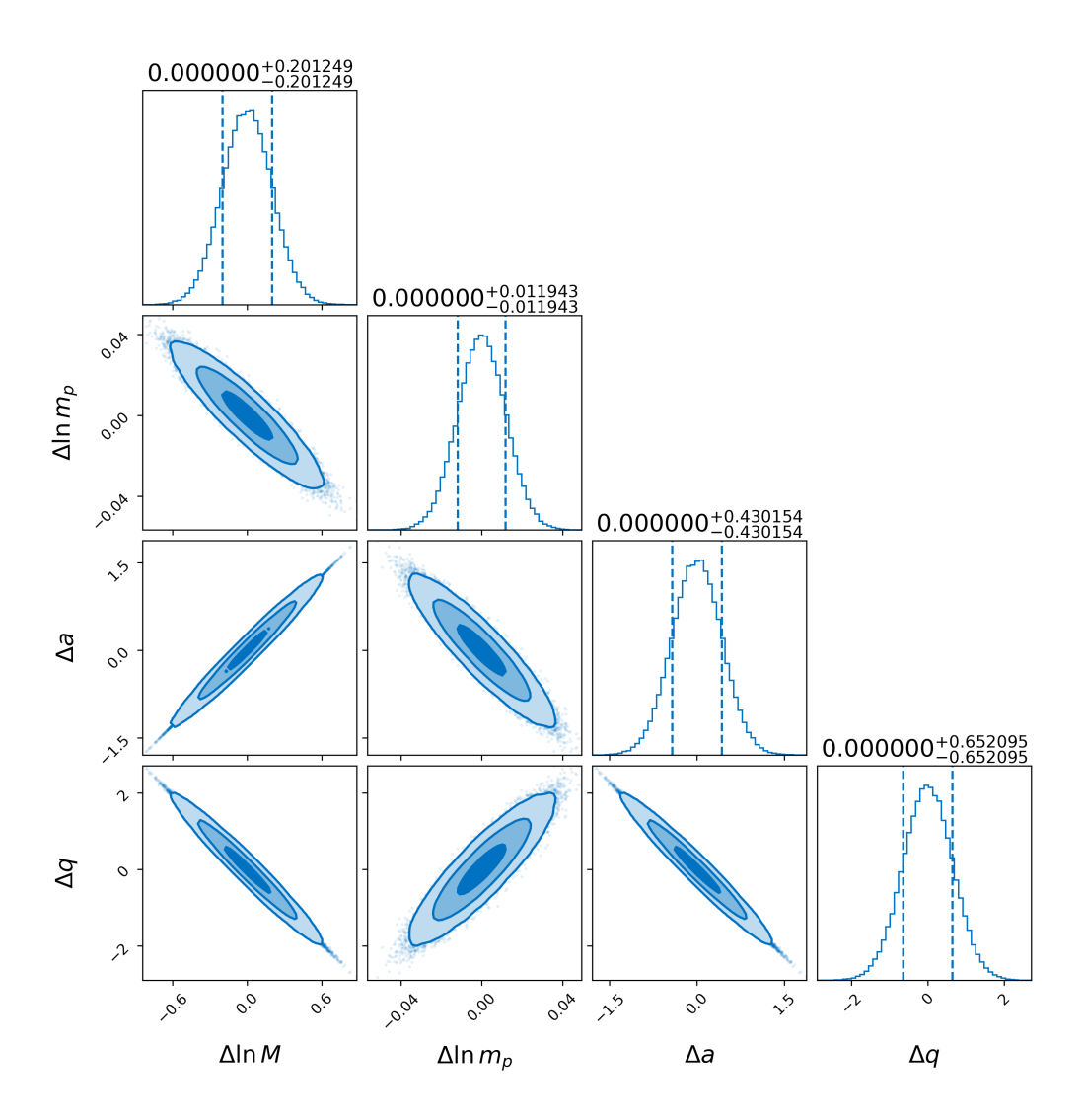


Figure 11. Corner plot for the probability distribution of the source parameters ($\ln M$, $\ln m_p$, a, q) with LISA, inferred after one-year observations of EMRIs with q=0.05 and a=-0.9. Vertical lines show the 1σ interval for the source parameter. The contours correspond to the 68%, 95%, and 99% probability confidence intervals.

the function $_{s}U(r)$ is

$$_{s}U(r) = _{s}U_{1}(r)\frac{\Delta}{(r^{2} + a^{2})^{2}} + _{s}G(r)^{2} + \frac{d_{s}G(r)}{dr}\frac{\Delta}{r^{2} + a^{2}} - \frac{\Delta_{s}G(r)_{s}F_{1}(r)}{r^{2} + a^{2}},$$
 (A.3)

$${}_sF_1(r) = \frac{\eta(r)_{,r}}{\eta(r)},\tag{A.4}$$

$$_{s}U_{1}(r) = V_{T} + \frac{1}{\beta \Delta^{s}} \left[\left(2\alpha + \beta_{,r} \Delta^{s+1} \right)_{,r} - \frac{\eta(r)_{,r}}{\eta(r)} \left(\alpha + \beta_{,r} \Delta^{s+1} \right) \right], \tag{A.5}$$

$$_sG(r) = \frac{r\Delta}{(r^2 + a^2)^2} + \frac{s(r-1)}{r^2 + a^2},$$
 (A.6)

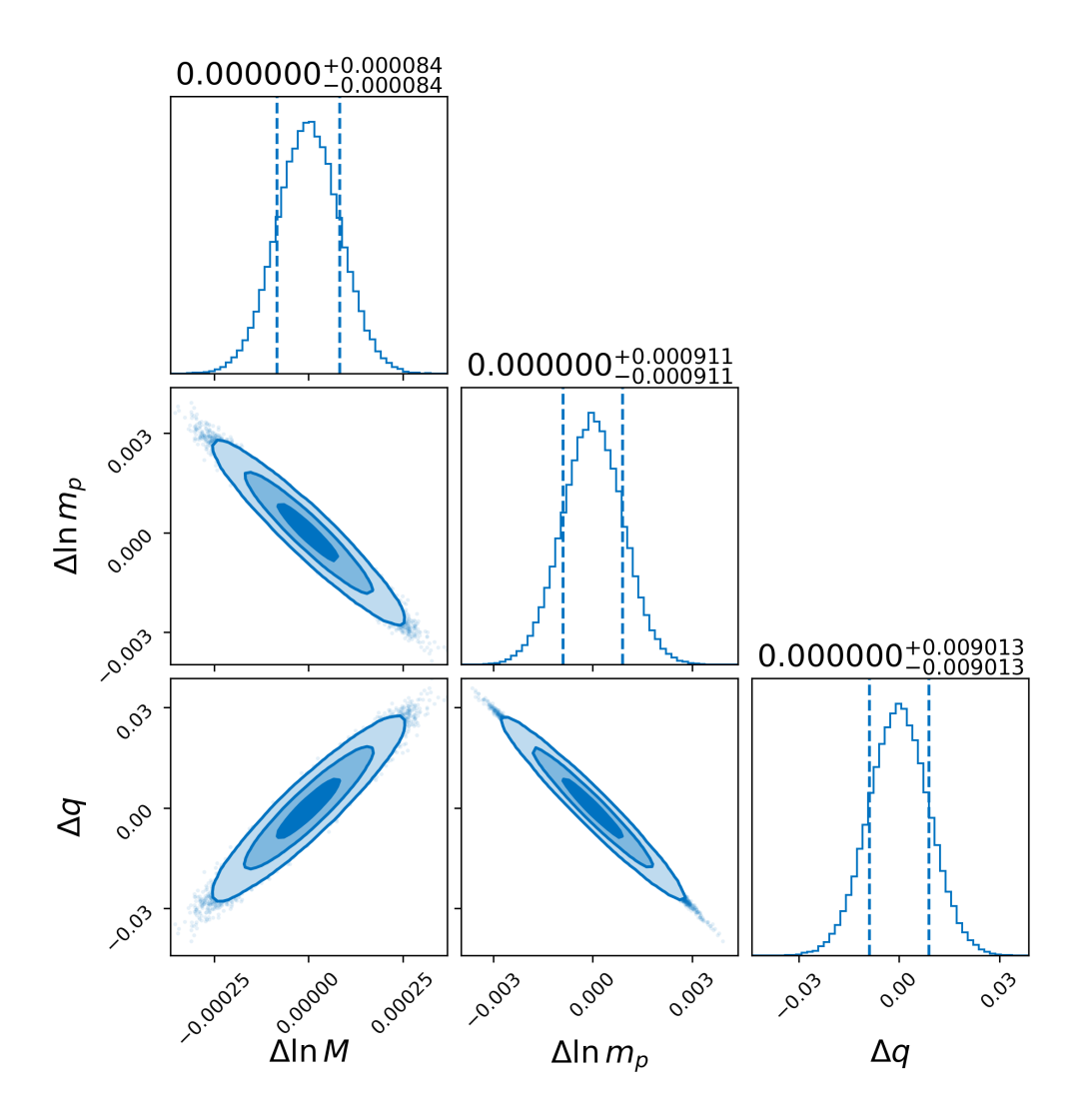


Figure 12. Corner plot for the probability distribution of the source parameters $(\ln M, \ln m_p, q)$ with LISA, inferred after one-year observations of EMRIs with q=0.05 in the Schwarzschild BH background. Vertical lines show the 1σ interval for the source parameter. The contours correspond to the 68%, 95%, and 99% probability confidence intervals.

where $_{,r}$ denotes the derivative with respect to r and

$$\eta(\hat{r}) = c_0 + \frac{c_1}{r} + \frac{c_2}{r^2} + \frac{c_3}{r^3} + \frac{c_4}{r^4}.$$
(A.7)

The solutions of the Teukolsky and generalized Sasaki-Nakamura equations are related by

$$R_{lm\omega}(r) = \frac{\left(\alpha + \beta_{,r}\Delta^{s+1}\right)\chi - \beta\Delta^{s+1}\chi'}{\eta},$$

$$\chi = \frac{X}{\sqrt{(r^2 + a^2)\Delta^s}}.$$
(A.8)

For s = -1,

$$c_{0} = -\lambda_{lm\omega},$$

 $c_{1} = -2iam,$
 $c_{2} = a^{2}(1 - 2\lambda_{lm\omega}),$
 $c_{3} = -2a^{2}(1 + iam),$
 $c_{4} = a^{4}(1 - \lambda_{lm\omega}),$
(A.9)

and

$$\alpha = \frac{(r^2 + a^2)}{r^2} \sqrt{\Delta} \left[-\frac{r}{r^2 + a^2} - \frac{iK}{\Delta} \right],$$

$$\beta = \frac{(r^2 + a^2)}{r^2} \sqrt{\Delta}.$$
(A.10)

The generalized Sasaki-Nakamura equation admits two linearly independent solutions, $X^{\rm in}_{lm\omega}$ and $X^{\rm up}_{lm\omega}$, with the asymptotic behaviour

$$X_{lm\omega}^{\rm in} \sim \begin{cases} e^{-i\kappa r^*} & r \to r_+ \\ A_{lm\omega}^{\rm out} e^{i\omega r^*} + A_{lm\omega}^{\rm in} e^{-i\omega r^*} & \hat{r} \to \infty \end{cases}, \tag{A.11}$$

$$X_{lm\omega}^{\rm up} \sim \begin{cases} C_{lm\omega}^{\rm out} e^{i\kappa r^*} + C_{lm\omega}^{\rm in} e^{-i\kappa r^*} & r \to r_+ \\ e^{i\omega r^*} & r \to \infty \end{cases}$$
 (A.12)

With the above normalization of the solutions $X_{lm\omega}^{\text{in}}$ $X_{lm\omega}^{\text{up}}$, the arbitrary constants D^{tran} and B^{tran} are determined as

$$D^{\text{tran}} = \frac{2i\omega}{\lambda_{lm\omega}},\tag{A.13}$$

$$B^{\text{tran}} = \frac{i\sqrt{\sqrt{1 - a^2 + 1}}}{4\sqrt{2}\left(2\left(\sqrt{1 - a^2 + 1}\right)\omega + i\sqrt{1 - a^2} - am\right)}.$$
 (A.14)

The numerical values of $X_{lm\omega}^{\rm in}$ ($X_{lm\omega}^{\rm up}$) are obtained by integrating Eq. (A.1) from r_+ (infinity) up to infinity (r_+) using the boundary conditions A.11 (A.12). We can derive the boundary conditions for the homogeneous generalized Sasaki-Nakamura equation in terms of explicit recursion relations which can be truncated at arbitrary order given by [101]. Then We transform $X_{lm\omega}^{\rm in}, X_{lm\omega}^{\rm up}$ back to the Teukolsky solutions $R_{lm\omega}^{\rm in}, R_{lm\omega}^{\rm up}$ using Eq. (A.8). The amplitude $B_{lm\omega}^{\rm in}$ can be obtained from the Wronskian W at a given orbital separation.

A.2 The source term

In this subsection, we give the explicit expressions for the source terms to compute the amplitudes $Z_{\omega lm}^{\infty,H}$ for equatorial circular orbital configurations. From Teukolsky's equation

(3.8) in [88], we get J_2

$$J_{2} = -\frac{3(a^{2} + (r - 2)r)}{2(r - ia\cos(\theta))^{2}(r + ia\cos(\theta))} J_{\bar{m}}$$

$$-\frac{-(a^{2} + r^{2})\partial_{t}J_{\bar{m}} + (a^{2} + (r - 2)r)\partial_{r}J_{\bar{m}} - a\partial_{\varphi}J_{\bar{m}}}{2(r - ia\cos(\theta))(r + ia\cos(\theta))}$$

$$+\frac{i\sin(\theta)(-2ar - 4ia^{2}\cos(\theta))}{\sqrt{2}(r - ia\cos(\theta))^{2}(r + ia\cos(\theta))} J_{n}$$

$$+\frac{i\sin(\theta)(a^{2}\cos(2\theta) + a^{2} + 2r^{2})(a\partial_{t}J_{n} + \csc^{2}(\theta)\partial_{\varphi}J_{n} + i\csc(\theta)\partial_{\theta}J_{n})}{2\sqrt{2}(r - ia\cos(\theta))^{2}(r + ia\cos(\theta))},$$
(A.15)

where $J_n = J^{\mu} n_{\mu}$ and $J_{\bar{m}} = J^{\mu} \bar{m}_{\mu}$. The source term $T_{\omega lm}$ for s = -1 is

$$T_{\omega lm}(r) = \frac{1}{2\pi} \int dt d\Omega \ 4\pi \Sigma T_{-1} S^{m}{}_{l}(\theta) e^{-im\varphi} e^{i\omega t}$$

$$= 2 \int dt d\Omega \ e^{i\omega t - im\varphi} \frac{r^{2} + a^{2} \cos^{2}(\theta)}{(r - ia \cos(\theta))^{-2}} {}_{-1} S^{m}{}_{l}(\theta) J_{2}.$$
(A.16)

The amplitudes $Z_{\omega lm}^{\infty,H}$ in Eq. (3.7) for s=-1 is

$$\int_{r_{+}}^{+\infty} \Delta^{-1} R_{\omega lm}^{\text{up,in}} T_{\omega lm} dr = \delta(\omega - m\hat{\omega}) \left[(I_{00} + I_{01}) R_{\omega lm}^{\text{up,in}} + I_{1} \frac{dR_{\omega lm}^{\text{up,in}}}{dr} \right], \tag{A.17}$$

where the coefficients are

$$I_{00} = \frac{\sqrt{2}\pi q \left(r_{-1} S^{m}_{l}'\left(\frac{\pi}{2}\right) + ia_{-1} S^{m}_{l}\left(\frac{\pi}{2}\right)\right)}{a\sqrt{r} + r^{2}},$$
(A.18)

$$I_{01} = -\sqrt{2}\pi q \,_{-1}S^{m}\,_{l}\left(\frac{\pi}{2}\right) \left[\frac{r\left(-r^{2}\omega + (r-2)\left(m\sqrt{r}+i\right)\right)}{\left(a^{2} + (r-2)r\right)\left(a+r^{3/2}\right)} + \frac{ia\left(a^{2} + a\sqrt{r}\left(1 + ir\omega\right) + r\left(-im\sqrt{r} - 2ir\omega + r - 2\right)\right)}{\sqrt{r}\left(a^{2} + (r-2)r\right)\left(a+r^{3/2}\right)}\right],$$
(A.19)

$$I_{1} = \frac{i\sqrt{2}\pi q\sqrt{r}\left(\sqrt{r} - a\right)}{a + r_{0}^{3/2}} {}_{-1}S^{m}{}_{l}\left(\frac{\pi}{2}\right). \tag{A.20}$$

References

- [1] LIGO SCIENTIFIC AND VIRGO COLLABORATIONS collaboration, Observation of Gravitational Waves from a Binary Black Hole Merger, Phys. Rev. Lett. 116 (2016) 061102 [1602.03837].
- [2] LIGO SCIENTIFIC AND VIRGO COLLABORATIONS collaboration, GW150914: The Advanced LIGO Detectors in the Era of First Discoveries, Phys. Rev. Lett. 116 (2016) 131103 [1602.03838].
- [3] LIGO SCIENTIFIC AND VIRGO COLLABORATIONS collaboration, GWTC-1: A Gravitational-Wave Transient Catalog of Compact Binary Mergers Observed by LIGO and Virgo during the First and Second Observing Runs, Phys. Rev. X 9 (2019) 031040 [1811.12907].

- [4] LIGO SCIENTIFIC AND VIRGO COLLABORATIONS collaboration, GWTC-2: Compact Binary Coalescences Observed by LIGO and Virgo During the First Half of the Third Observing Run, Phys. Rev. X 11 (2021) 021053 [2010.14527].
- [5] LIGO SCIENTIFIC AND VIRGO COLLABORATIONS collaboration, GWTC-2.1: Deep Extended Catalog of Compact Binary Coalescences Observed by LIGO and Virgo During the First Half of the Third Observing Run, 2108.01045.
- [6] LIGO SCIENTIFIC, VIRGO AND KAGRA COLLABORATIONS collaboration, GWTC-3: Compact Binary Coalescences Observed by LIGO and Virgo During the Second Part of the Third Observing Run, 2111.03606.
- [7] LIGO SCIENTIFIC AND VIRGO COLLABORATIONS collaboration, GW170817: Observation of Gravitational Waves from a Binary Neutron Star Inspiral, Phys. Rev. Lett. 119 (2017) 161101 [1710.05832].
- [8] LIGO SCIENTIFIC AND VIRGO COLLABORATIONS collaboration, GW190425: Observation of a Compact Binary Coalescence with Total Mass $\sim 3.4 M_{\odot}$, Astrophys. J. Lett. 892 (2020) L3 [2001.01761].
- [9] LIGO SCIENTIFIC, KAGRA AND VIRGO COLLABORATIONS collaboration, Observation of Gravitational Waves from Two Neutron Star-Black Hole Coalescences, Astrophys. J. Lett. 915 (2021) L5 [2106.15163].
- [10] K. Danzmann, LISA: An ESA cornerstone mission for a gravitational wave observatory, Class. Quant. Grav. 14 (1997) 1399.
- [11] LISA collaboration, Laser Interferometer Space Antenna, 1702.00786.
- [12] TianQin collaboration, TianQin: a space-borne gravitational wave detector, Class. Quant. Grav. 33 (2016) 035010 [1512.02076].
- [13] W.-R. Hu and Y.-L. Wu, The Taiji Program in Space for gravitational wave physics and the nature of gravity, Natl. Sci. Rev. 4 (2017) 685.
- [14] Y. Gong, J. Luo and B. Wang, Concepts and status of Chinese space gravitational wave detection projects, Nature Astron. 5 (2021) 881 [2109.07442].
- [15] TianQin collaboration, The TianQin project: current progress on science and technology, PTEP 2021 (2021) 05A107 [2008.10332].
- [16] W.-H. Ruan, Z.-K. Guo, R.-G. Cai and Y.-Z. Zhang, Taiji program: Gravitational-wave sources, Int. J. Mod. Phys. A 35 (2020) 2050075 [1807.09495].
- [17] LISA collaboration, Astrophysics with the Laser Interferometer Space Antenna, Living Rev. Rel. 26 (2023) 2 [2203.06016].
- [18] LISA collaboration, New horizons for fundamental physics with LISA, Living Rev. Rel. 25 (2022) 4 [2205.01597].
- [19] P. Amaro-Seoane, J.R. Gair, M. Freitag, M. Coleman Miller, I. Mandel, C.J. Cutler et al., Astrophysics, detection and science applications of intermediate- and extreme mass-ratio inspirals, Class. Quant. Grav. 24 (2007) R113 [astro-ph/0703495].
- [20] S. Babak, J. Gair, A. Sesana, E. Barausse, C.F. Sopuerta, C.P.L. Berry et al., Science with the space-based interferometer LISA. V: Extreme mass-ratio inspirals, Phys. Rev. D 95 (2017) 103012 [1703.09722].
- [21] L. Barack and C. Cutler, LISA capture sources: Approximate waveforms, signal-to-noise ratios, and parameter estimation accuracy, Phys. Rev. D 69 (2004) 082005 [gr-qc/0310125].
- [22] A.J.K. Chua, C.J. Moore and J.R. Gair, Augmented kludge waveforms for detecting extreme-mass-ratio inspirals, Phys. Rev. D 96 (2017) 044005 [1705.04259].

- [23] J.R. Gair, C. Tang and M. Volonteri, LISA extreme-mass-ratio inspiral events as probes of the black hole mass function, Phys. Rev. D 81 (2010) 104014 [1004.1921].
- [24] D.E. Holz and S.A. Hughes, *Using gravitational-wave standard sirens*, *Astrophys. J.* **629** (2005) 15 [astro-ph/0504616].
- [25] C.L. MacLeod and C.J. Hogan, Precision of Hubble constant derived using black hole binary absolute distances and statistical redshift information, Phys. Rev. D 77 (2008) 043512 [0712.0618].
- [26] D. Laghi, N. Tamanini, W. Del Pozzo, A. Sesana, J. Gair, S. Babak et al., Gravitational-wave cosmology with extreme mass-ratio inspirals, Mon. Not. Roy. Astron. Soc. 508 (2021) 4512 [2102.01708].
- [27] LISA COSMOLOGY WORKING GROUP collaboration, Cosmology with the Laser Interferometer Space Antenna, 2204.05434.
- [28] ELISA collaboration, The Gravitational Universe, 1305.5720.
- [29] K. Eda, Y. Itoh, S. Kuroyanagi and J. Silk, New Probe of Dark-Matter Properties: Gravitational Waves from an Intermediate-Mass Black Hole Embedded in a Dark-Matter Minispike, Phys. Rev. Lett. 110 (2013) 221101 [1301.5971].
- [30] K. Eda, Y. Itoh, S. Kuroyanagi and J. Silk, Gravitational waves as a probe of dark matter minispikes, Phys. Rev. D 91 (2015) 044045 [1408.3534].
- [31] E. Barausse, V. Cardoso and P. Pani, Can environmental effects spoil precision gravitational-wave astrophysics?, Phys. Rev. D 89 (2014) 104059 [1404.7149].
- [32] X.-J. Yue and W.-B. Han, Gravitational waves with dark matter minispikes: the combined effect, Phys. Rev. D 97 (2018) 064003 [1711.09706].
- [33] X.-J. Yue, W.-B. Han and X. Chen, Dark matter: an efficient catalyst for intermediate-mass-ratio-inspiral events, Astrophys. J. 874 (2019) 34 [1802.03739].
- [34] C.P.L. Berry, S.A. Hughes, C.F. Sopuerta, A.J.K. Chua, A. Heffernan, K. Holley-Bockelmann et al., *The unique potential of extreme mass-ratio inspirals for gravitational-wave astronomy*, 1903.03686.
- [35] O.A. Hannuksela, K.C.Y. Ng and T.G.F. Li, Extreme dark matter tests with extreme mass ratio inspirals, Phys. Rev. D 102 (2020) 103022 [1906.11845].
- [36] K. Destounis, A.G. Suvorov and K.D. Kokkotas, Testing spacetime symmetry through gravitational waves from extreme-mass-ratio inspirals, Phys. Rev. D 102 (2020) 064041 [2009.00028].
- [37] J.Y.J. Burton and T. Osburn, Reissner-Nordström perturbation framework with gravitational wave applications, Phys. Rev. D 102 (2020) 104030 [2010.12984].
- [38] T. Torres and S.R. Dolan, Electromagnetic self-force on a charged particle on Kerr spacetime: Equatorial circular orbits, Phys. Rev. D 106 (2022) 024024 [2008.12703].
- [39] E. Barausse et al., Prospects for Fundamental Physics with LISA, Gen. Rel. Grav. 52 (2020) 81 [2001.09793].
- [40] V. Cardoso and A. Maselli, Constraints on the astrophysical environment of binaries with gravitational-wave observations, Astron. Astrophys. 644 (2020) A147 [1909.05870].
- [41] A. Maselli, N. Franchini, L. Gualtieri and T.P. Sotiriou, *Detecting scalar fields with Extreme Mass Ratio Inspirals*, *Phys. Rev. Lett.* **125** (2020) 141101 [2004.11895].
- [42] A. Maselli, N. Franchini, L. Gualtieri, T.P. Sotiriou, S. Barsanti and P. Pani, Detecting fundamental fields with LISA observations of gravitational waves from extreme mass-ratio inspirals, Nature Astron. 6 (2022) 464 [2106.11325].

- [43] H. Guo, Y. Liu, C. Zhang, Y. Gong, W.-L. Qian and R.-H. Yue, Detection of scalar fields by extreme mass ratio inspirals with a Kerr black hole, Phys. Rev. D 106 (2022) 024047 [2201.10748].
- [44] C. Zhang, Y. Gong, D. Liang and B. Wang, Gravitational waves from eccentric extreme mass-ratio inspirals as probes of scalar fields, 2210.11121.
- [45] S. Barsanti, N. Franchini, L. Gualtieri, A. Maselli and T.P. Sotiriou, Extreme mass-ratio inspirals as probes of scalar fields: Eccentric equatorial orbits around Kerr black holes, Phys. Rev. D 106 (2022) 044029 [2203.05003].
- [46] S. Barsanti, A. Maselli, T.P. Sotiriou and L. Gualtieri, Detecting massive scalar fields with Extreme Mass-Ratio Inspirals, 2212.03888.
- [47] V. Cardoso, K. Destounis, F. Duque, R.P. Macedo and A. Maselli, Black holes in galaxies: Environmental impact on gravitational-wave generation and propagation, Phys. Rev. D 105 (2022) L061501 [2109.00005].
- [48] N. Dai, Y. Gong, T. Jiang and D. Liang, Intermediate mass-ratio inspirals with dark matter minispikes, Phys. Rev. D 106 (2022) 064003 [2111.13514].
- [49] T. Jiang, N. Dai, Y. Gong, D. Liang and C. Zhang, Constraint on Brans-Dicke theory from intermediate/extreme mass ratio inspirals, JCAP 12 (2022) 023 [2107.02700].
- [50] C. Zhang and Y. Gong, Detecting electric charge with extreme mass ratio inspirals, Phys. Rev. D 105 (2022) 124046 [2204.08881].
- [51] Q. Gao, Constraint on the mass of graviton with gravitational waves, Sci. China Phys. Mech. Astron. 66 (2023) 220411 [2206.02140].
- [52] Q. Gao, Y. You, Y. Gong, C. Zhang and C. Zhang, Testing alternative theories of gravity with space-based gravitational wave detectors, 2212.03789.
- [53] K. Destounis, A. Kulathingal, K.D. Kokkotas and G.O. Papadopoulos, Gravitational-wave imprints of compact and galactic-scale environments in extreme-mass-ratio binaries, 2210.09357.
- [54] D. Liang, R. Xu, Z.-F. Mai and L. Shao, Probing vector hair of black holes with extreme mass ratio inspirals, 2212.09346.
- [55] V. Cardoso, C.F.B. Macedo and R. Vicente, Eccentricity evolution of compact binaries and applications to gravitational-wave physics, Phys. Rev. D 103 (2021) 023015 [2010.15151].
- [56] L. Liu, O. Christiansen, Z.-K. Guo, R.-G. Cai and S.P. Kim, Gravitational and electromagnetic radiation from binary black holes with electric and magnetic charges: Circular orbits on a cone, Phys. Rev. D 102 (2020) 103520 [2008.02326].
- [57] L. Liu, O. Christiansen, W.-H. Ruan, Z.-K. Guo, R.-G. Cai and S.P. Kim, Gravitational and electromagnetic radiation from binary black holes with electric and magnetic charges: elliptical orbits on a cone, Eur. Phys. J. C 81 (2021) 1048 [2011.13586].
- [58] V. Cardoso, K. Destounis, F. Duque, R. Panosso Macedo and A. Maselli, Gravitational Waves from Extreme-Mass-Ratio Systems in Astrophysical Environments, Phys. Rev. Lett. 129 (2022) 241103 [2210.01133].
- [59] T.P. Sotiriou and S.-Y. Zhou, Black hole hair in generalized scalar-tensor gravity, Phys. Rev. Lett. 112 (2014) 251102 [1312.3622].
- [60] H.O. Silva, J. Sakstein, L. Gualtieri, T.P. Sotiriou and E. Berti, Spontaneous scalarization of black holes and compact stars from a Gauss-Bonnet coupling, Phys. Rev. Lett. 120 (2018) 131104 [1711.02080].

- [61] D.D. Doneva and S.S. Yazadjiev, New Gauss-Bonnet Black Holes with Curvature-Induced Scalarization in Extended Scalar-Tensor Theories, Phys. Rev. Lett. 120 (2018) 131103 [1711.01187].
- [62] G. Antoniou, A. Bakopoulos and P. Kanti, Evasion of No-Hair Theorems and Novel Black-Hole Solutions in Gauss-Bonnet Theories, Phys. Rev. Lett. 120 (2018) 131102 [1711.03390].
- [63] N. Yunes, P. Pani and V. Cardoso, Gravitational Waves from Quasicircular Extreme Mass-Ratio Inspirals as Probes of Scalar-Tensor Theories, Phys. Rev. D 85 (2012) 102003 [1112.3351].
- [64] V. Cardoso, S. Chakrabarti, P. Pani, E. Berti and L. Gualtieri, Floating and sinking: The Imprint of massive scalars around rotating black holes, Phys. Rev. Lett. 107 (2011) 241101 [1109.6021].
- [65] G.W. Gibbons, Vacuum Polarization and the Spontaneous Loss of Charge by Black Holes, Commun. Math. Phys. 44 (1975) 245.
- [66] D.M. Eardley and W.H. Press, Astrophysical processes near black holes, Ann. Rev. Astron. Astrophys. 13 (1975) 381.
- [67] R.S. Hanni, Limits on the charge of a collapsed object, Phys. Rev. D 25 (1982) 2509.
- [68] P.S. Joshi and J.V. Narlikar, Limits of the charge of a collapsed object., Pramana 18 (1982) 385.
- [69] Y. Gong, Z. Cao, H. Gao and B. Zhang, On neutralization of charged black holes, Mon. Not. Roy. Astron. Soc. 488 (2019) 2722 [1907.05239].
- [70] J.D. Bekenstein, Hydrostatic Equilibrium and Gravitational Collapse of Relativistic Charged Fluid Balls, Phys. Rev. D 4 (1971) 2185.
- [71] F. de Felice, Y. Yu and J. Fang, Relativistic charged spheres, Mon. Not. Roy. Astron. Soc. 277 (1995) L17.
- [72] F. de Felice, S.-m. Liu and Y.-q. Yu, Relativistic charged spheres. 2. Regularity and stability, Class. Quant. Grav. 16 (1999) 2669 [gr-qc/9905099].
- [73] B.V. Ivanov, Static charged perfect fluid spheres in general relativity, Phys. Rev. D 65 (2002) 104001 [gr-qc/0203070].
- [74] S.D. Majumdar, A class of exact solutions of Einstein's field equations, Phys. Rev. 72 (1947) 390.
- [75] J.L. Zhang, W.Y. Chau and T.Y. Deng, The influence of a net charge on the critical mass of a neutron star, Astrophys. Space Sci. 88 (1982) 81.
- [76] P. Anninos and T. Rothman, *Instability of extremal relativistic charged spheres*, *Phys. Rev. D* **65** (2002) 024003 [gr-qc/0108082].
- [77] W.B. Bonnor and S.B.P. Wickramasuriya, Are very large gravitational redshifts possible, Mon. Not. Roy. Astron. Soc. 170 (1975) 643.
- [78] S. Ray, A.L. Espindola, M. Malheiro, J.P.S. Lemos and V.T. Zanchin, Electrically charged compact stars and formation of charged black holes, Phys. Rev. D 68 (2003) 084004 [astro-ph/0307262].
- [79] R.M. Wald, Black hole in a uniform magnetic field, Phys. Rev. D 10 (1974) 1680.
- [80] V. Cardoso, C.F.B. Macedo, P. Pani and V. Ferrari, Black holes and gravitational waves in models of minicharged dark matter, JCAP 05 (2016) 054 [1604.07845].

- [81] J.S. Bolton, A. Caputo, H. Liu and M. Viel, Comparison of Low-Redshift Lyman-α Forest Observations to Hydrodynamical Simulations with Dark Photon Dark Matter, Phys. Rev. Lett. 129 (2022) 211102 [2206.13520].
- [82] L. Liu and S.P. Kim, Merger rate of charged black holes from the two-body dynamical capture, JCAP 03 (2022) 059 [2201.02581].
- [83] L. Liu, Z.-K. Guo, R.-G. Cai and S.P. Kim, Merger rate distribution of primordial black hole binaries with electric charges, Phys. Rev. D 102 (2020) 043508 [2001.02984].
- [84] P. Jai-akson, A. Chatrabhuti, O. Evnin and L. Lehner, Black hole merger estimates in Einstein-Maxwell and Einstein-Maxwell-dilaton gravity, Phys. Rev. D 96 (2017) 044031 [1706.06519].
- [85] O. Christiansen, J. Beltrán Jiménez and D.F. Mota, Charged Black Hole Mergers: Orbit Circularisation and Chirp Mass Bias, Class. Quant. Grav. 38 (2021) 075017 [2003.11452].
- [86] G. Bozzola and V. Paschalidis, General Relativistic Simulations of the Quasicircular Inspiral and Merger of Charged Black Holes: GW150914 and Fundamental Physics Implications, Phys. Rev. Lett. 126 (2021) 041103 [2006.15764].
- [87] T. Zi, Z. Zhou, H.-T. Wang, P.-C. Li, J.-d. Zhang and B. Chen, Analytic kludge waveforms for extreme-mass-ratio inspirals of a charged object around a Kerr-Newman black hole, Phys. Rev. D 107 (2023) 023005 [2205.00425].
- [88] S.A. Teukolsky, Perturbations of a rotating black hole. 1. Fundamental equations for gravitational electromagnetic and neutrino field perturbations, Astrophys. J. 185 (1973) 635.
- [89] W.H. Press and S.A. Teukolsky, Perturbations of a Rotating Black Hole. II. Dynamical Stability of the Kerr Metric, Astrophys. J. 185 (1973) 649.
- [90] S.A. Teukolsky and W.H. Press, Perturbations of a rotating black hole. III Interaction of the hole with gravitational and electromagnet ic radiation, Astrophys. J. 193 (1974) 443.
- [91] E.T. Newman and R. Penrose, Note on the Bondi-Metzner-Sachs group, J. Math. Phys. 7 (1966) 863.
- [92] J.N. Goldberg, A.J. MacFarlane, E.T. Newman, F. Rohrlich and E.C.G. Sudarshan, Spin-s spherical harmonics and \eth , J. Math. Phys. 8 (1967) 2155.
- [93] "Black Hole Perturbation Toolkit." (bhptoolkit.org).
- [94] S.L. Detweiler, Black Holes and Gravitational Waves. I. Circular Orbits About a Rotating Hole, Astrophys. J. 225 (1978) 687.
- [95] S.A. Hughes, The Evolution of circular, nonequatorial orbits of Kerr black holes due to gravitational wave emission, Phys. Rev. D 61 (2000) 084004 [gr-qc/9910091].
- [96] P.I. Jefremov, O.Y. Tsupko and G.S. Bisnovatyi-Kogan, Innermost stable circular orbits of spinning test particles in Schwarzschild and Kerr space-times, Phys. Rev. D 91 (2015) 124030 [1503.07060].
- [97] E. Berti, A. Buonanno and C.M. Will, Estimating spinning binary parameters and testing alternative theories of gravity with LISA, Phys. Rev. D 71 (2005) 084025 [gr-qc/0411129].
- [98] L. Lindblom, B.J. Owen and D.A. Brown, Model Waveform Accuracy Standards for Gravitational Wave Data Analysis, Phys. Rev. D 78 (2008) 124020 [0809.3844].
- [99] K. Chatziioannou, A. Klein, N. Yunes and N. Cornish, Constructing Gravitational Waves from Generic Spin-Precessing Compact Binary Inspirals, Phys. Rev. D 95 (2017) 104004 [1703.03967].
- [100] S.A. Hughes, Computing radiation from Kerr black holes: Generalization of the Sasaki-Nakamura equation, Phys. Rev. D 62 (2000) 044029 [gr-qc/0002043].

[101] G.A. Piovano, A. Maselli and P. Pani, Extreme mass ratio inspirals with spinning secondary: a detailed study of equatorial circular motion, Phys. Rev. D 102 (2020) 024041 [2004.02654].